

5

Branched Manifolds

5.1	Closed Loops	166
5.3	What Has This Got to Do with Dynamical Systems?	169
5.3	General Properties of Branched Manifolds	169
5.4	Birman–Williams Theorem	171
5.5	Relaxation of Restrictions	175
5.6	Examples of Branched Manifolds	176
5.7	Uniqueness and Nonuniqueness	186
5.8	Standard Form	190
5.9	Topological Invariants	193
5.10	Additional Properties	199
5.11	Subtemplates	207
5.12	Summary	215

All of the unstable periodic orbits in a strange attractor can be placed on a single, simple geometric structure. This structure has been called variously a *knot holder*, an *orbit organizer*, and a *template*. Mathematically, it is a branched manifold. A branched manifold describes the topological organization of all the unstable periodic orbits in a strange attractor [83,84]. This means that the branched manifold for a strange attractor provides information about the stretching and squeezing mechanisms that generate the strange attractor. Branched manifolds can be classified discretely. This means that a discrete classification exists for low-dimensional strange attractors [85].

5.1 CLOSED LOOPS

Branched manifolds are central to the classification theory for strange attractors of low dimensional dynamical systems. In this section we introduce the idea of branched manifolds in an amusing but very nontrivial way.

5.1.1 Undergraduate Students

Many of us in physics or electrical engineering departments have had to teach Maxwell's equations in one form or another. One standard problem that we always give to undergraduates is to compute the magnetic field generated by a current carrying wire. Needless to say, the wire is straight and the current is constant. The standard approach is to find a closed loop, or magnetic field line, and perform a Gaussian type integral around it. As Fig. 5.1(a) shows, there is a two (continuous)-parameter family of closed field lines around the wire. These are parameterized by distance along the wire and radius of the loop.

5.1.2 Graduate Students

Through sheer perversity, we always make our students go through another round of electricity and magnetism in graduate school. The material is the same, but the problems have to be different—and harder. This time around, we bend the straight wire into a circular loop and then ask our students to compute the magnetic field in its vicinity. As Fig. 5.1(b) shows, there is still a real two-parameter family of closed loops around the current-carrying wire. One parameter is the angular distance around the wire; the other is the *perihelion* of the closed magnetic field line with respect to the current-carrying wire. The perihelion is the distance of closest approach. Some students (the smart ones) choose not to solve the problem with this approach.

5.1.3 The Ph.D. Candidate

When the poor student finally finishes his (her) thesis, you may be put on his committee. If you like the student, you give easy questions. If not, you give impossible questions.

Here is one. You take the current-carrying wire and tie it into a knot: a figure 8 knot, to be specific. Then ask: Are there still closed magnetic field lines? If so, what are they like?

It turns out that most of the closed field lines of undergraduate and graduate days break when the current-carrying wire is tied into the figure 8 knot. However, a few do not break. "Few" is, in fact, a countable infinity—significantly fewer than a continuous two-parameter family.

Not only are the closed magnetic field lines countable, they can also be named. More surprisingly, they are organized among themselves in a rigid and surprisingly simple way. The organizational mechanism is illustrated in Fig. 5.2. The current-carrying wire, tied into a figure 8 knot, is shown in Fig. 5.2(a). One of the closed

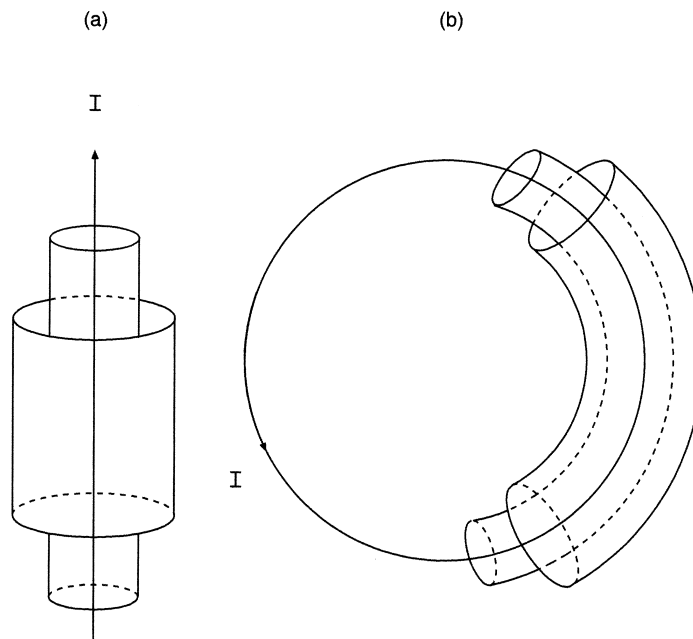


Fig. 5.1 (a) The closed magnetic field lines surrounding a straight wire carrying a uniform constant current can be identified by two real continuous parameters. (b) This remains true if the wire is deformed into a closed circular loop.

field lines generated by the current in this wire is shown in Fig. 5.2(b). In Fig. 5.2(c) we show a structure that contains all the information about the organization of all the closed magnetic field lines generated by the current in this wire. This structure is a branched manifold (or knot-holder, or template).

All of the closed field lines surrounding the Figure 8 knot can be deformed (*isotoped*) down to lie on this two-dimensional surface without undergoing any self-intersections. On this surface it is a relatively simple matter to compute the topological invariants of these closed field lines, their linking numbers. There is a 1:1 correspondence between symbol sequences for closed paths along the “one-way streets” (branches) in this branched manifold and the closed magnetic field lines surrounding the current-carrying wire. The symbols may identify either the branch lines, as encountered, or the branches of the branched manifold, as traversed. As a result, the closed field lines are clearly countable.

5.1.4 Important Observation

We point out here, forcefully, that this first encounter with branched manifolds has occurred for a “conservative” dynamical system.

In the past it seems that there has been a prejudice against the use of branched manifolds as a valuable tool for classifying strange attractors. This prejudice had been brought about by the incorrect assumption that this tool is useful only in the highly dissipative limit. The central tool for the classification theory, the Birman–Williams theorem, is applicable to dissipative three-dimensional dynamical systems ($\lambda_1 + \lambda_2 + \lambda_3 < 0$), but these systems need not be highly dissipative.

In the example just discussed, a branched manifold describes the organization of all the closed magnetic field lines around a current-carrying figure 8 knot. The analog dynamical system is *conservative*, not even *slightly dissipative*.

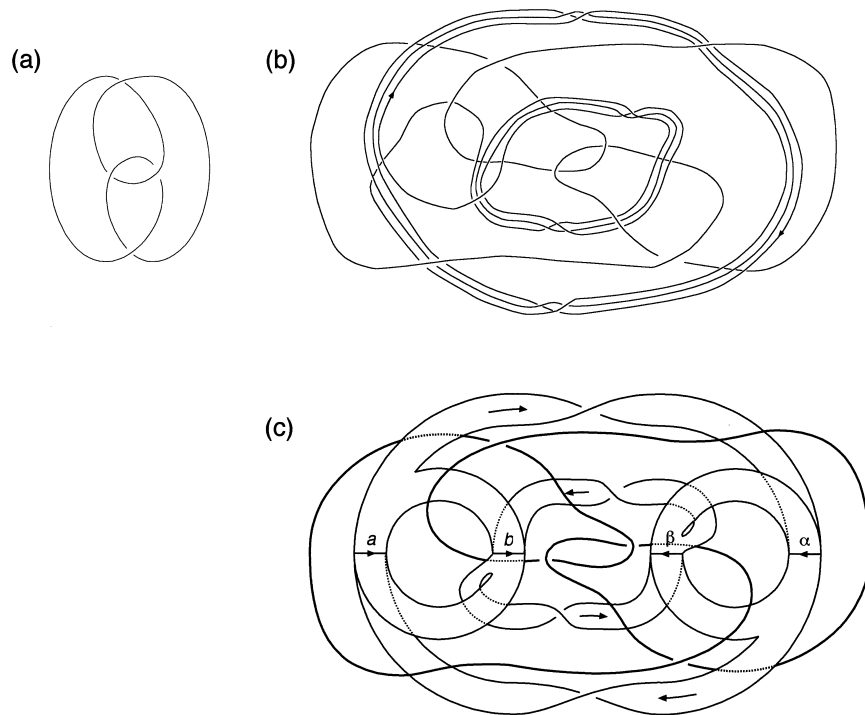


Fig. 5.2 A current-carrying wire tied into a figure 8 knot (a) generates a countable number of closed magnetic field lines, one of which is shown in part (b). (c) This branched manifold describes all of the closed field lines generated by the wire in (a). It can also be used to label all these orbits, and to compute their topological invariants, such as linking numbers. The closed loop shown in (b) can be identified as $(a\alpha)^3 a (b\beta)^3 b$. Adapted with permission from Birman and Williams [84].

5.2 WHAT HAS THIS GOT TO DO WITH DYNAMICAL SYSTEMS?

We are interested in classifying dynamical systems by the strange attractors that they generate. When a dynamical system in R^3 generates a chaotic signal, a large number of periodic orbits occur in the strange attractor. They are organized among themselves in a unique way. This organization reflects the stretching and squeezing mechanisms, which act to generate chaotic behavior.

There is a theorem, due to Birman and Williams, which guarantees that all these orbits can be isotoped down to a two-dimensional branched manifold, preserving their topological organization. As a result, we can identify a dynamical system by the branched manifold that describes the periodic orbits in its strange attractor.

The Birman–Williams theorem is valid for dissipative dynamical systems in R^3 . The Lyapunov exponents for the strange attractor obey $\lambda_1 > 0$, $\lambda_2 = 0$, and $\lambda_3 < 0$, with $\lambda_1 + \lambda_2 + \lambda_3 < 0$. The Lyapunov dimension of such an attractor is $d_L = 2 + (\lambda_1 + \lambda_2)/|\lambda_3| = 2 + \epsilon$. When $\epsilon = \lambda_1/|\lambda_3|$ is small, it is easy to discern the shape of the branched manifold from the numerically computed strange attractor [cf. Figs. 5.7(c) and 5.8(c)]. However, when $\epsilon \simeq 1$ there is still a branched manifold which describes the dynamics, even though it may not be easy to identify from the strange attractor.

We emphasize once again that the branched manifold for the figure 8 knot describes the topological organization of the closed field lines in a system which has the properties of a strange attractor with $\epsilon = 1$: the conservative limit.

5.3 GENERAL PROPERTIES OF BRANCHED MANIFOLDS

The branched manifold shown in Fig. 5.2(c) consists of two kinds of structures. These describe stretching and squeezing. The origin of these structures is shown in Fig. 5.3. On the left we show a cube of initial conditions. Under the stretching process, the cube is deformed: It stretches in one direction and contracts in the other. Eventually, the flow goes off in two different directions in phase space. In the limit of very high dissipation, the three-dimensional structure becomes two-dimensional. This structure describes stretching.

On the right we show two neighborhoods in different parts of phase space. Under the flow they are squeezed together. Between the two deformed neighborhoods there is a boundary layer. In the limit of very high dissipation, the three-dimensional structure becomes two-dimensional. This structure describes squeezing.

Remark: The two-dimensional structures shown at the bottom of Fig. 5.3 do not depend on the dissipation being large. They, in fact, result from projecting the flow down along the stable direction. We emphasize again that the construction of branched manifolds does not depend on the dissipation being large.

The most general branched manifold is built up from just these two building blocks in Lego fashion. The simple rules are:

Out \rightarrow **in**: Every outflow feeds into an inflow.

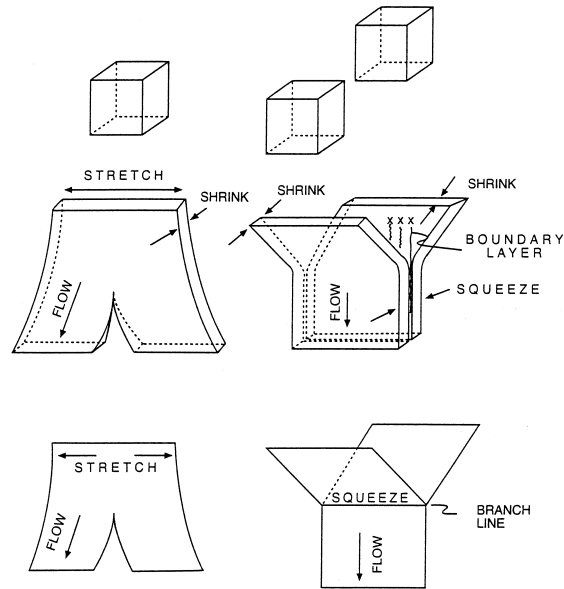


Fig. 5.3 Left: A cube of initial conditions (top) is deformed under the stretching part of the flow (middle). A gap begins to form for two parts of the flow heading to different parts of phase space. Under further shrinking (higher dissipation) a two-dimensional structure is formed which is not a manifold because of the tear point, which is an initial condition for a trajectory to a singular point. Right: Two cubes of initial conditions (top) in distant parts of phase space are squeezed together and deformed by the flow (middle). A boundary layer separates the deformed parallelepipeds at their junction. Under more dissipation the two inflow regions are joined to the outflow region by a branch line.

No free ends: There are no uncoupled outflow or inflow edges.

The two-dimensional branched manifolds that we use to classify dynamical systems are two-dimensional manifolds *almost* everywhere. Of the two dimensions: one dimension corresponds to the flow direction; the other corresponds to the unstable invariant manifold of a low-period orbit. The structure fails to be a manifold because of singularities. There are two types of singularities:

Zero-dimensional: The splitting points identify stretching mechanisms.

One-dimensional: The branch lines identify squeezing mechanisms.

It is possible to describe branched manifolds algebraically. The algebraic description for a branched manifold with n branches has three components:

Topological Matrix T : This is an $n \times n$ matrix that describes the topological organization of the branches. The diagonal element T_{ii} describes the local torsion

of branch i . This is the signed number of crossings of the two edges of branch i with each other. The off-diagonal elements $T_{ij} = T_{ji}$ describe how branches i and j cross. The crossing convention adopted for segments of orbits (Fig. 4.4) is extended to projections of the branches in an obvious way.

Joining Array A: This is a $1 \times n$ array that describes the order in which branches are joined at branch lines. A simple convention is: The closer a branch is to the observer, the lower the branch number.

Incidence Matrix I: This is an $n \times n$ transition or incidence matrix. It describes which branches flow into which branches. If branch i flows into branch j , then $I_{ij} = 1$; it is zero otherwise.

The algebraic description for the branched manifold shown in Fig. 5.2(c) is given in Fig. 5.4.

We remark here that the algebraic description of a branched manifold is not unique. The branched manifold is embedded in R^3 . As such, it can be rotated and projected to a variety of two-dimensional surfaces. Different projections have different algebraic representations. This nonuniqueness is the nonuniqueness of projections, discussed in Section 4.2.1. There are several other ways in which branched manifolds for an underlying dynamics may not be unique. However, there is one invariant: They all describe the same spectrum of periodic orbits with the same topological organization.

We also remark here that the algebraic description of branched manifolds is ideally suited for the computation of some topological invariants, such as linking numbers and relative rotation rates, but is not suitable for computing other invariants, such as knot polynomials.

5.4 BIRMAN–WILLIAMS THEOREM

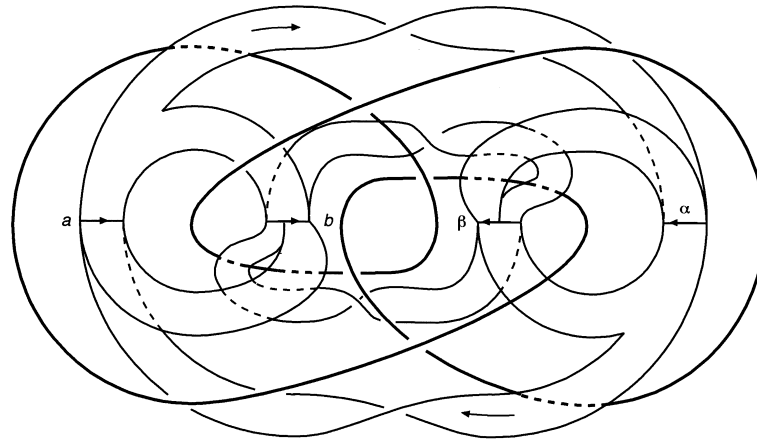
We refer the interested reader to [83] and [84] for proof of the Birman–Williams theorem. In the first subsection we introduce the projection method (Birman–Williams projection) that is used to project a flow onto a branched manifold. In the second subsection we state the Birman–Williams theorem.

5.4.1 Birman–Williams Projection

Two points, x and y , are defined to be *equivalent* under a flow if they have the same asymptotic future:

$$x \sim y \quad \text{if} \quad |x(t) - y(t)| \xrightarrow{t \rightarrow \infty} 0 \quad (5.1)$$

The Birman–Williams projection (5.1) has the effect of projecting the flow in a strange attractor down along the stable direction onto a two-dimensional branched manifold. The dimensions include the flow direction and part of the unstable direction. It is illustrated in Fig. 5.5.



(b) $a\alpha \quad ab \quad b\beta \quad ba \mid aa \quad a\beta \quad \beta b \quad \beta\alpha$ (c) $a\alpha \quad ab \quad b\beta \quad ba \mid aa \quad a\beta \quad \beta b \quad \beta\alpha$

$a\alpha$	-1								
ab	0								
$b\beta$		$+1$	$+1$						
ba		$+1$	0						
aa				-1					
$a\beta$					0				
βb						$+1$	$+1$		
$\beta\alpha$						$+1$	0		
									$[-4 \quad -1 \quad +3 \quad -2 \mid +2 \quad -3 \quad +1 \quad -4]$

$a\alpha$			1	1					
ab			1	1					
$b\beta$							1	1	
ba	1	1							
aa				1	1				
$a\beta$							1	1	
βb				1	1				
$\beta\alpha$				1	1				

Fig. 5.4 Algebraic representation of a branched manifold with n branches (a) consists of: (b) an $n \times n$ matrix T that describes how the branches cross over or under each other (off-diagonal matrix elements) or how they twist about their flow axis (diagonal matrix elements), and underneath this matrix a $1 \times n$ array A that describes the order in which the branches join each other at branch lines, with the convention: The larger the number, the farther behind; and in addition, an $n \times n$ matrix I (incidence matrix) (c) describes how the branches are connected to each other. The branches may be labeled by numbers or by indicating which branch lines they connect. Adapted with permission from Birman and Williams [84].

We represent the flow in R^3 by Φ_t , so that for x in the basin of the strange attractor \mathcal{SA} , $\Phi_t(x(0)) = x(t)$. The flow has a unique future and past; that is, given $x(0)$, the points $x(t)$ are determined uniquely for all t in the range $-\infty < t < +\infty$.

The Birman–Williams projection maps every point x in the basin of \mathcal{SA} into a point \bar{x} in a branched manifold \mathcal{BM} . This projection is illustrated in Fig. 5.6. This figure shows how a flow that exhibits a stretch and fold mechanism [Fig. 5.6(a)] is transformed into a pair of branches that meet at a branch line [Fig. 5.6(b)]. The projection also maps the flow Φ_t in the basin of \mathcal{SA} to a semiflow $\bar{\Phi}_t$ on \mathcal{BM} . Under the semiflow, every point $\bar{x} \in \mathcal{BM}$ has a unique future $\bar{x}(t)$. Every point \bar{x} also has

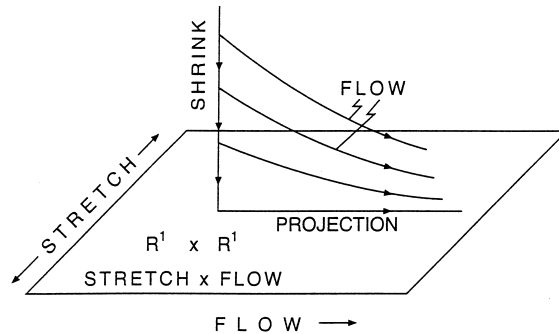


Fig. 5.5 The Birman–Williams projection identifies all points with the same asymptotic future. This has the effect of projecting the flow in a low-dimensional strange attractor down onto a two-dimensional manifold almost everywhere.

a unique past up to the first branch line in its past. At the branch line, information about its previous history is lost.

It is useful to extend each splitting point back to the nearest branch line in its past, as shown in Fig. 5.4. Then each branch line is split into a number of segments. Each branch of the branched manifold can then be labeled by the segments of the branches that it connects. These two symbols, the first the source, the second the sink, can be used to label the rows and columns of the transition matrix I .

Every point in a branched manifold has a unique future. In particular, every point on a branch line has a unique future. The future may be:

Aperiodic: A nonrepeating, chaotic orbit of infinite period.

Periodic: A periodic or ultimately orbit of finite period p .

Roughly speaking, each branch line can be considered to be like the closed interval $[0, 1]$. The points on a branch line that are initial conditions for aperiodic orbits are like the irrational numbers, and the points on a branch line that are initial conditions for periodic or ultimately periodic orbits are like the rational numbers. Both point sets are dense on the interval. We refine this classification slightly in Section 5.9.1.

5.4.2 Statement of the Theorem

The Birman–Williams theorem is as follows [83, 84]:

Theorem: Assume that a flow Φ_t :

- On R^3 is dissipative ($\lambda_1 > 0, \lambda_2 = 0, \lambda_3 < 0$ and $\lambda_1 + \lambda_2 + \lambda_3 < 0$).
- Generates a hyperbolic strange attractor \mathcal{SA} .

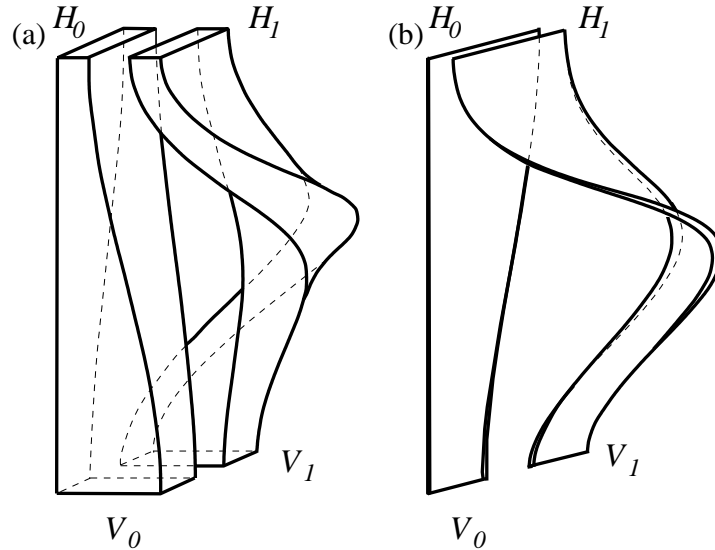


Fig. 5.6 (a) Suspension of the horseshoe map represented as a continuous deformation of the two “vertical” rectangles V_0 and V_1 of Fig. 2.19 into the “horizontal” rectangles H_0 and H_1 , with time flowing from bottom to top. Top and bottom should be identified. (b) When the flow is squeezed along the stable direction (i.e., dissipation is increased to infinity), the two prisms in (a) are transformed into a pair of two-dimensional branches that meet at a branch line. A complete branched manifold is obtained by connecting the branch line to the bottom with a flat ribbon.

The projection (5.1) maps the strange attractor \mathcal{SA} to a branched manifold \mathcal{BM} and the flow Φ_t on \mathcal{SA} in R^3 to a semiflow $\bar{\Phi}_t$ on \mathcal{BM} in R^3 . The periodic orbits in \mathcal{SA} under Φ_t correspond 1:1 with the periodic orbits in \mathcal{BM} under $\bar{\Phi}_t$, with perhaps one or two specified exceptions. On any finite subset of periodic orbits the correspondence can be taken to be via isotopy.

This means, roughly but accurately, that the flow Φ_t on \mathcal{SA} can be deformed continuously to the flow $\bar{\Phi}_t$ on \mathcal{BM} . During this deformation, periodic orbits are neither created nor destroyed, and orbit segments do not pass through each other (there are no crossings). In addition, their topological organization, as described by their linking numbers, remains invariant.

5.5 RELAXATION OF RESTRICTIONS

There are two serious restrictions on the Birman–Williams theorem. They have been underlined in the statement of the theorem. If they were unavoidable, they would render the theorem much less useful for experimental applications than it actually is. In this section we describe how these restrictions can be circumvented.

5.5.1 Strongly Contracting Restriction

The very first application of the Birman–Williams theorem to a physical system [1] ran into an unexpected and fortuitous problem. This involved the analysis of experimental data taken from a chemical system, the oscillating Belousov–Zhabotinskii reaction. Every theoretical description of this reaction involved more than three variables [86]. The Birman–Williams theorem is valid for three-dimensional systems. Knots fall apart in dimensions higher than 3. So, in principle, it appears that both the theorem and knowledge of the periodic orbits of this system are useless.

Despite this, we were able to carry out a successful analysis of the data and determine a branched manifold which described the organization of all the periodic orbits that we were able to extract from the experimental data.

Why?

This success in the face of inapplicable theorems leads to a deeper understanding of the Birman–Williams theorem, and more generally of low-dimensional strange attractors. First, the data do not care about the theoretical description (such descriptions are often incorrect, anyway). Suppose that the data are embedded in n dimensions and the Lyapunov exponents obey

$$\lambda_1 > \lambda_2 = 0 > \lambda_3 > \dots > \lambda_n \quad (5.2)$$

Assume also that the attractor is *strongly* contracting. By definition, this means that

$$\lambda_1 + \lambda_2 + \lambda_3 < 0 \quad (5.3)$$

Then the Birman–Williams projection can be carried out in two steps. First, the projection is carried out along the strongly contracting directions corresponding to $\lambda_4, \lambda_5, \dots, \lambda_n$. This has the effect of projecting the flow in R^n into a three-dimensional manifold, \mathcal{IM} . The manifold \mathcal{IM} is called an *inertial manifold*. In this three-dimensional manifold:

- The conditions of the Birman–Williams theorem are met.
- The topological organization of periodic orbits is defined (knots don't fall apart).

The last projection along the least stable direction (λ_3) maps $\mathcal{SA} \subset \mathcal{IM}$ down to a two-dimensional branched manifold $\mathcal{BM} \subset \mathcal{IM}$ and preserves the topological organization of the unstable periodic orbits in the strange attractor.

For strongly contracting flows, the Lyapunov dimension

$$d_L = 2 + \frac{\lambda_1}{|\lambda_3|} < 3 \quad (5.4)$$

is less than 3. More specifically, if $d_L(x)$ is the local Lyapunov dimension at $x \in \mathcal{SA}$, and if $d_L(x) < 3$ everywhere on \mathcal{SA} , the Birman–Williams projection (5.1) provides a projection of $\mathcal{SA} \subset R^n$ down to a two-dimensional branched manifold $\mathcal{BM} \subset \mathcal{IM}^3 \subset R^n$, where \mathcal{IM}^3 is the three-dimensional manifold that results from the projection along the strongly stable directions $\lambda_j, j = 4, \dots, n$.

5.5.2 Hyperbolic Restriction

We have never encountered a hyperbolic strange attractor, either in experimental data or in numerical simulations of ordinary differential equations.

Speaking roughly but accurately once again, the condition of hyperbolicity guarantees that the strange attractor is structurally stable under perturbations: Periodic orbits are neither created nor destroyed under perturbation of the control parameters. We get around this problem by assuming hyperbolicity for the strange attractor of interest. In doing so, we predict the existence of many more periodic orbits than actually exist in the strange attractor. Then we “unfold” the attractor. This means that we find a family of dynamical systems depending on one or (usually) more control parameters. The family contains the hyperbolic attractor for some control parameter value. Then we change the values of the control parameters. Under these changes many periodic orbits can be destroyed. However, the orbits that remain during the unfolding are organized in exactly the same way as in the hyperbolic attractor.

Unfolding comes in two forms. There is a global version and a local version. In the local version, as control parameters are changed, the branches in the branched manifold remain unchanged: It is the spectrum of periodic orbits on these branches that changes. In fact, the possible changes are restricted by topological considerations, as described in Sections 4.2 and 4.3. If we push the control parameters too far, new branches can come into existence and old branches can go out of existence. This is seen clearly in the perestroika of the Duffing oscillator and is visible in the experimental data described in Chapter 7. Unfoldings are discussed extensively in Chapter 9.

5.6 EXAMPLES OF BRANCHED MANIFOLDS

In this section we classify each of the four dynamical systems described in Section 3.3. This is done by integrating the dynamical equations for certain parameter values and then identifying the branched manifold which describes the strange attractor generated by each of these sets of equations. Precisely how the identification is made is discussed in detail in Chapter 6, which presents the topological analysis algorithm. We emphasize the fact that the branched manifold may change as the control parameters are varied. The possible changes are discussed more extensively in Chapter 9, which deals with unfoldings. A large number of branched manifolds are described in [87].

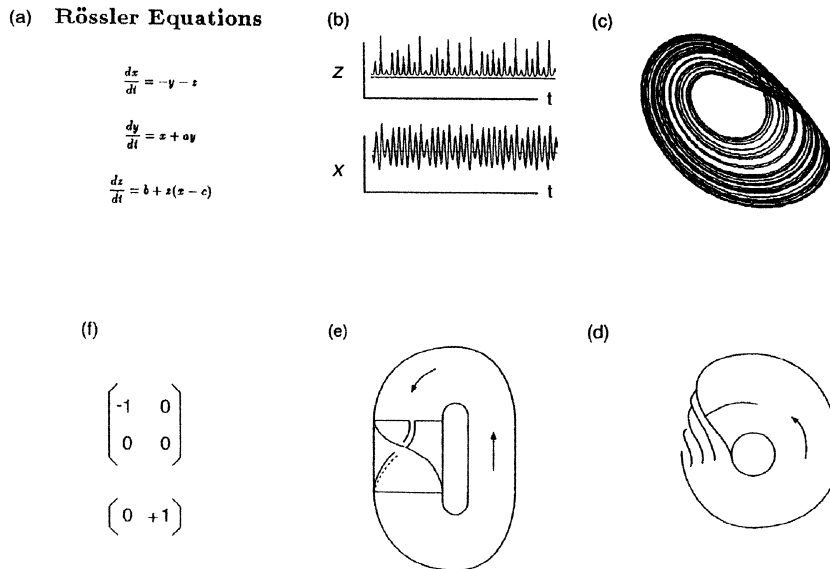


Fig. 5.7 (a) Rössler equations (3.22). (b) $x(t)$ and $z(t)$ after the transients have died out and the trajectory has relaxed to the strange attractor. Control parameter values: $(a, b, c) = (0.398, 2.0, 4.0)$. (c) Projection of the strange attractor onto the x - y plane. (d) Caricature of the flow on the attractor. (e) Branched manifold for this attractor. (f) Algebraic representation of this branched manifold. The topological matrix is shown at the top and the array at the bottom.

5.6.1 Smale–Rössler System

The Smale horseshoe mechanism consists of simple stretching and folding in phase space. It occurs very frequently in experiments that exhibit chaotic behavior [1, 78, 88–92]. This mechanism is exhibited by the Rössler equations.

The classification of the Rössler dynamical system is illustrated in Fig. 5.7 [2]. This figure consists of six parts. The equations of motion are shown in Fig. 5.7(a). These equations were integrated for control parameter values $(a, b, c) = (0.398, 2.0, 4.0)$. The traces $x(t)$ and $z(t)$ are recorded in Fig. 5.7(b). They were recorded after the transients died out. That is, an initial condition in the basin of attraction was chosen, and the integration was carried out beyond the point at which the trajectory relaxed to the strange attractor before the recording was begun. Figure 5.7(c) shows the attractor as projected onto the x - y plane $z = 0$. The flow is counterclockwise. The fold occurs at the 12 o'clock position (these comments are for analog people only). During the fold, the outer part of the attractor at the 5 o'clock position folds over the top of the inner part of the flow.

A schematic representation of this flow is presented in Fig. 5.7(d). It is clear that Fig. 5.7(d) is not a totally accurate representation of the dynamics shown in Fig. 5.7(c). In Fig. 5.7(d) the outer edge of the flow is reinjected to the inner edge of the flow, whereas in Fig. 5.7(c) the outer and inner edges of the flow at the 5 o'clock (or 9 o'clock) position are not squeezed together. As a result, the branched manifold shown in Fig. 5.7(d) contains more periodic orbits than actually exist in the flow shown in Fig. 5.7(c). However, the periodic orbits that exist in Fig. 5.7(c) are organized in exactly the same way as they are in Fig. 5.7(d).

The branched manifold is shown in a standard (*braid*) representation in Fig. 5.7(e). In this standard representation, all of the stretching and squeezing occurs between the two horizontal lines shown on the left-hand side. These two lines are branch lines—in fact, the same branch line. The flow emerging from the branch line at the bottom is returned to the branch line at the top without undergoing stretching and squeezing. It is no exaggeration to claim that all the nonlinear mechanisms responsible for chaotic motion are expressed between these two branch lines.

The algebraic representation for the branched manifolds in Fig. 5.7(d) and (e) is given in Fig. 5.7(f). There are two branches. Each branch contains one period-1 orbit. The 2×2 matrix T provides topological information. The diagonal elements describe the torsion of the two branches. The off-diagonal matrix elements T_{ij} are twice the linking number of the period-1 orbits in the branches i and j : $T_{ij} = 2L(i, j)$. The 1×2 array provides information about how the branches are ordered when they join at the branch line. In this case, the left-hand branch lies over the right-hand branch (in this projection). Its index is lower than the index for the right-hand branch, according to the convention adopted. The flow represented by this branched manifold is fully expansive. The incidence matrix I is therefore full: $\begin{bmatrix} 1 & 1 \\ 1 & 1 \end{bmatrix}$. When the incidence matrix is full, it is generally not presented explicitly.

Before leaving this dynamical system, we make a few observations about qualitative behavior. A small change in control parameter values will generally produce a small modification in Fig. 5.7(c); that is, there will be only a small change in how the two bands overlap. This results in only a small change in the spectrum of unstable periodic orbits in the attractor. If we continue to push the control parameters in an appropriate direction, the attractor will grow bigger. The outer edge will extend farther from the center, and when folded over, it will come closer to the center. One might easily believe that the folded-over region will never reach the center. If true, at some point the approach to the center will reverse itself. When this occurs, a second fold will occur at the inner edge of the attractor. In short, a third branch will be created. This third branch is connected to the second branch [-1 in Fig. 5.7(f)]. By continuity arguments, one might expect that its local torsion could only have values differing from -1 by ± 1 . We could also expect that the local torsion value would place constraints on how this new branch could join with the two existing branches. These suspicions are true. It is in this way that the classification of strange attractors by branched manifolds allows us to make predictions about the behavior of nonlinear dynamical systems under perturbations both small and large.

5.6.2 Lorenz System

The Lorenz mechanism consists of a tear and a squeeze in phase space. It occurs in experiments that exhibit chaotic behavior and have some twofold symmetry.

The classification of the Lorenz dynamical system is illustrated in Fig. 5.8 [2]. This figure is identical in structure to Fig. 5.7 for the Rössler system. It consists of six parts. The Lorenz equations are shown in Fig. 5.8(a). These equations were integrated for control parameter values $(b, \sigma, r) = (\frac{8}{3}, 10.0, 30.0)$. The traces $x(t)$ and $z(t)$ are recorded in Fig. 5.8(b) after transients have died out. Figure 5.8(c) shows the attractor as projected onto the $x = y$ vs. z plane. The flow is clockwise on the left and counterclockwise on the right. The squeeze and tear occur in the middle.

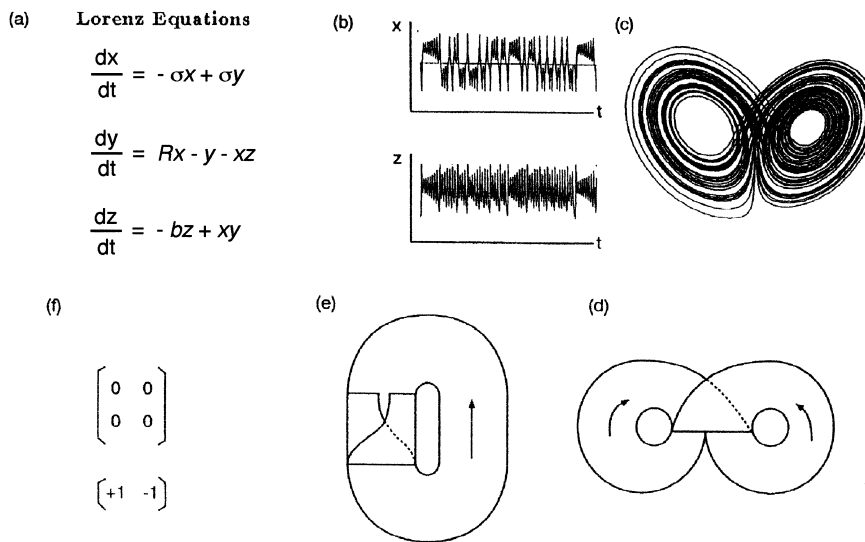


Fig. 5.8 (a) Lorenz equations (3.20). (b) $x(t)$ and $z(t)$ plotted after transients have died out and the trajectory has relaxed to the strange attractor. Control parameter values: $(b, \sigma, r) = (\frac{8}{3}, 10.0, 30.0)$. (c) Projection of the strange attractor onto the $x = y-z$ plane. (d) Caricature of the flow on the attractor. (e) Branched manifold for this attractor. (f) Algebraic representation for this branched manifold. The topological matrix is shown at the top and the array at the bottom.

A schematic representation of this flow is presented in Fig. 5.8(d) and has been deformed into the branched manifold shown in Fig. 5.8(e). Once again, the stretching and squeezing mechanisms responsible for generating chaotic behavior are contained between the two horizontal lines.

The algebraic representation for the branched manifolds in Fig. 5.8(d) and (e) is given in Fig. 5.8(f). Neither branch exhibits twist, and the period-1 orbits in each branch correspond, in fact, to the two unstable foci. They clearly do not link.

The topological matrix appears trivial (all matrix elements are zero); nevertheless, it describes highly nontrivial dynamics. The array describes the order in which the two branches are connected. The incidence matrix is full, indicating that each branch flows into both.

Once again, the branched manifold description of this dynamics introduces the possibility of making educated guesses as to the behavior under control parameter variation. That is, one might expect the two outer edges to fold over when reinjected to the interior of the flow on the “opposite side.” When new branches are visited by the flow (in symmetric pairs), they can only be related to the previously existing branches in a limited number of ways.

5.6.3 Duffing System

The dynamics of the Duffing oscillator are governed by a simple stretch and fold mechanism, in much the same way as in the Rössler system. However, unlike the Rössler oscillator, the Duffing oscillator has a twofold symmetry. As a result, the dynamics of the Duffing oscillator and its description by means of branched manifolds are much richer than those of the Rössler oscillator.

We describe the Duffing oscillator more thoroughly in Chapter 10, but in principle, what happens is simple. During the first half of a cycle, phase space undergoes a stretch and fold. The fold may be simple or may not be simple (i.e., multiple nondegenerate folds may occur). An identical stretch and fold occurs during the second half of the cycle. As a result, Duffing dynamics are the “square” of Rössler dynamics. More precisely, they are essentially Rössler dynamics twice iterated.

In Fig. 5.9 we present the branched manifold (to be accurate, only the central part, between the two horizontal lines in the standard representation) which describes an *extended fold*. This type of mechanism occurs for the Rössler equations for suitable control parameter values [2,93]. What we show in this figure is a branched manifold with four branches. This branched manifold is obtained as follows. A branch line, shown at the top right, is stretched out by a factor of 4 (i.e., $e^{\lambda_1} = 4$). This stretched branch line is then rolled up (right, middle) and then squeezed back down to the original interval (right, bottom). The four period-1 orbits in these dynamics are shown by symbols x in this figure. The four branches in this branched manifold are labeled by their local torsion, which varies systematically from 0 to 3 on going from left to right. It is relatively simple to verify that the linking numbers of the period-1 orbits in the four branches satisfy $L(i, j) = 1$ if $i \neq 0$ and $j \neq 0$, and are zero otherwise. These simple calculations define the 16 elements of the topological matrix. The array can be read off from the scrolling action shown on the right (see especially the middle figure on the right). The template and its algebraic representation are shown on the left in this figure.

In the Duffing oscillator this *scroll and squeeze mechanism* occurs twice. We illustrate this mechanism in Fig. 5.10 for the case where the stretch is by a factor of 3 in each half of a cycle. At the top of Fig. 5.10 we show a branch line. It is divided into three equal parts, labeled 1, 2, 3. These integers indicate twist during the first half cycle. Each part is further subdivided into three equal parts. During

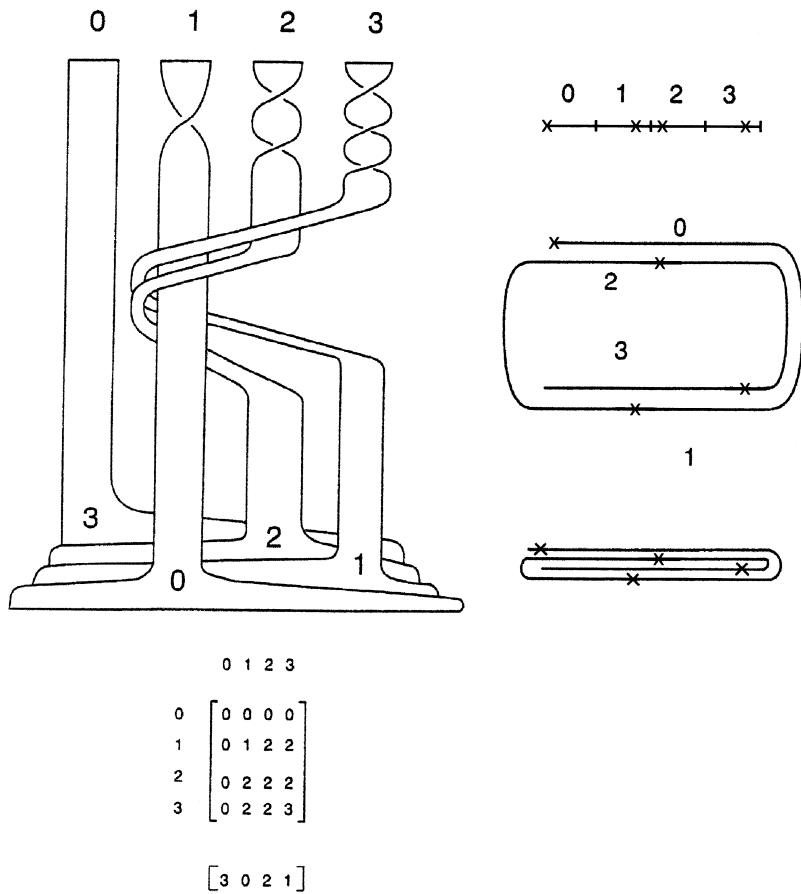


Fig. 5.9 Extended folding, as seen in the Rössler attractor for some control parameter values. Right: A branch line (top) is stretched by a factor of 4, rolled around like a jellyroll (middle), and then squeezed (bottom). The resulting branched manifold (left, top) and its algebraic representation (left, bottom) are then easily constructed.

the first half cycle this branch line is stretched out and rolled to a configuration as shown in Fig. 5.9, containing only branches 1, 2, and 3. This deformed branch line is then rotated through π radians, and then squeezed. The rotation accounts for the symmetry $(x, y, t) \rightarrow (-x, -y, t + \frac{1}{2}T)$ during half a cycle. This process is then repeated. The nine branches are conveniently labeled by two symbols: $(1,1), (1,2), \dots, (2,3), (2,2), \dots, (3,3)$. The nine period-1 orbits for this iterated threefold stretch-and-roll mechanism can be located as indicated in Fig. 5.9, and their linking numbers computed. The ordering of the branches can be identified by inspection. This leads

directly to the 9×9 topological matrix and the 1×9 array given at the bottom of Fig. 5.10.

Although the branched manifold and its algebraic description appear very complicated, both are generated by very simple rules. In particular, it is a simple matter to predict what happens when suitable control parameters are varied. New branches can be added and old branches removed only in a systematic and predictable way.

5.6.4 van der Pol System

We discuss a version of the van der Pol equations studied by Shaw [94, 95]:

$$\begin{aligned}\dot{x} &= -0.7y + x(1 - 10y^2) \\ \dot{y} &= +x - 0.25 \sin(2\pi t/T)\end{aligned}\tag{5.5}$$

The van der Pol oscillator exhibits the same half-period symmetry as the Duffing oscillator: The equations (5.5) are invariant under $(x, y, t) \rightarrow (-x, -y, t + \frac{1}{2}T)$, where T is the period of the driving term. The strange attractor generated by these equations must exhibit the same invariance. We therefore creep up on the description of this strange attractor in two steps, as we did for the branched manifold of the Duffing oscillator. We first describe what happens during half a period. Then we iterate.

Up to now, the branch lines we have encountered have been intervals—segments of R^1 . However, it is only necessary that the branch line be one-dimensional. In the case of the van der Pol oscillator the branch line(s) is a segment with endpoints identified, a circle S^1 . This comes about because the van der Pol oscillator undergoes a Hopf bifurcation on its way to chaos. The intersection of the strange attractor with a Poincaré section can be embedded in an annulus. Under the Birman–Williams projection, the annulus is mapped to S^1 , and under the (semi)flow, S^1 is mapped to S^1 .

Under the flow, stretching takes place. Stretching is followed by folding. However, only an even number of folds can occur, because of the global boundary conditions. In Fig. 5.11(a) we show both a branched manifold that describes the flow and a return map of S^1 to itself [Fig. 5.11(b)]. It is clear from this figure that two folds must occur (more generally, folds must be paired). The standard representation of a branched manifold is shown in Fig. 5.11(c). This is obtained by splitting open the flow shown in Fig. 5.11(a) and identifying the edges of the flow. The algebraic description for this flow is shown in Fig. 5.11(d). The discontinuity of local torsion for contiguous branches, as shown by the diagonal matrix elements of the topological matrix, is intimately related to the global boundary conditions (S^1 instead of R^1).

Figure 5.11 describes a strange attractor generated by a stretch and fold mechanism acting on an annulus but without the twofold symmetry exhibited by the van der Pol oscillator [2]. To construct a branched manifold for the van der Pol oscillator, the mechanism shown in Fig. 5.11 must be appropriately iterated. We illustrate what happens, in some range of control parameters, in Fig. 5.12. If the pinching during the first half cycle occurs at the top, the pinching during the second half cycle must occur at the bottom to account properly for the inversion part of the symmetry

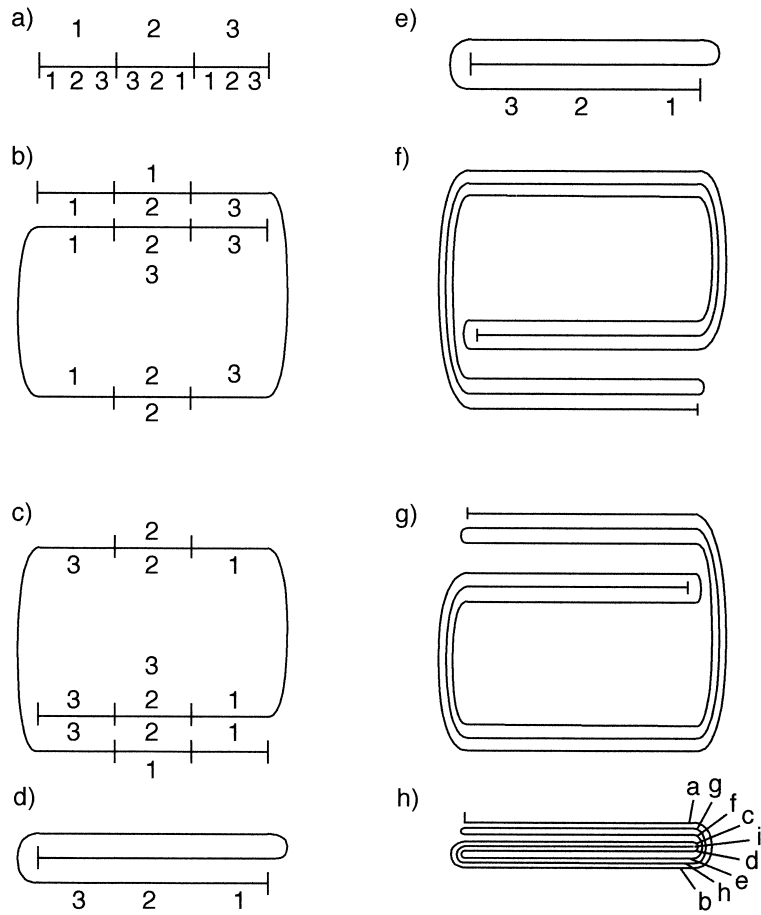


Fig. 5.10 The stretching and squeezing mechanism for the Duffing oscillator is essentially the second iterate of the stretch and fold mechanism for the extended Smale horseshoe, with suitable modifications. Stretching and squeezing during the first half cycle is shown on the left. The second half cycle is shown on the right. (a) A branch line with three large segments is shown. Each segment is divided into three smaller segments. All are labeled as shown. (b) The branch line is stretched by a factor of 3 and scrolled. (c) The stretched branch line is rotated by π radians in the direction of the scroll rotation and squeezed (d). (e) The squeezed branch line is again stretched by a factor of 3 and scrolled (f) and rotated by π radians (g) and squeezed (h). The period-1 orbits can be located by the method indicated in Fig. 5.9 and their linking numbers computed. The local torsion of the period-1 orbit through branch (i, j) is $i + j$. This information is sufficient to construct the topological matrix. Array information can be read directly from (g) or (h).

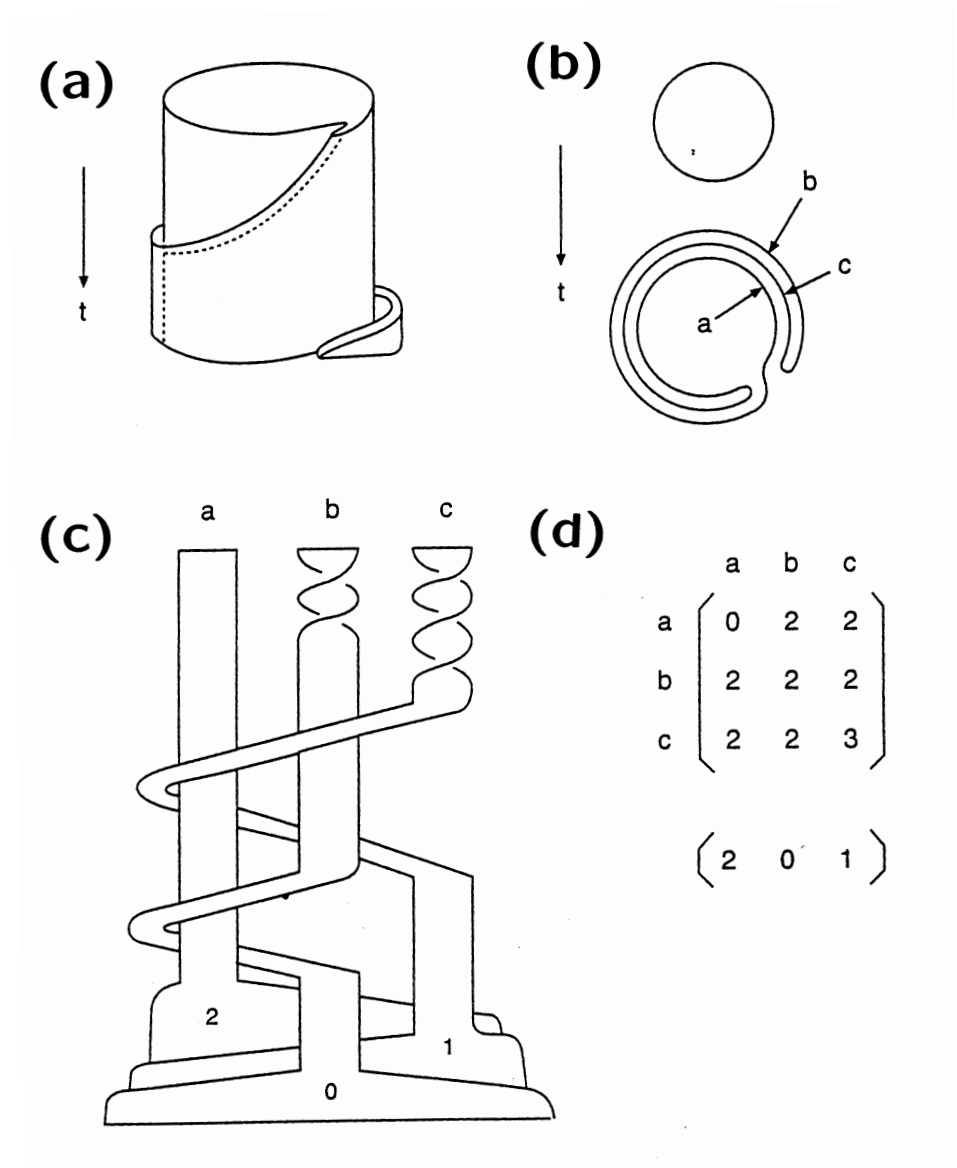


Fig. 5.11 What happens during half a cycle in the van der Pol oscillator. (a) The flow along the cylinder is pinched out, deformed, and folded back to the cylinder. The branched manifold is shown on the left. (b) The return map of the branch line S^1 is a circle map. (c) The flow in (a) is slit open, showing three branches for the branched manifold. (d) The topological matrix and array can be determined by inspection. The discontinuity of local torsions for contiguous branches is a signature that nonlocal boundary conditions must be imposed.

$[(x, y) \rightarrow -(x, y)]$. In this iteration, a total of nine branches is created. In Fig. 5.12 we present a caricature (cartoon) of this van der Pol mechanism which is similar to that presented in Fig. 5.10 for the mechanism at work in the Duffing oscillator.

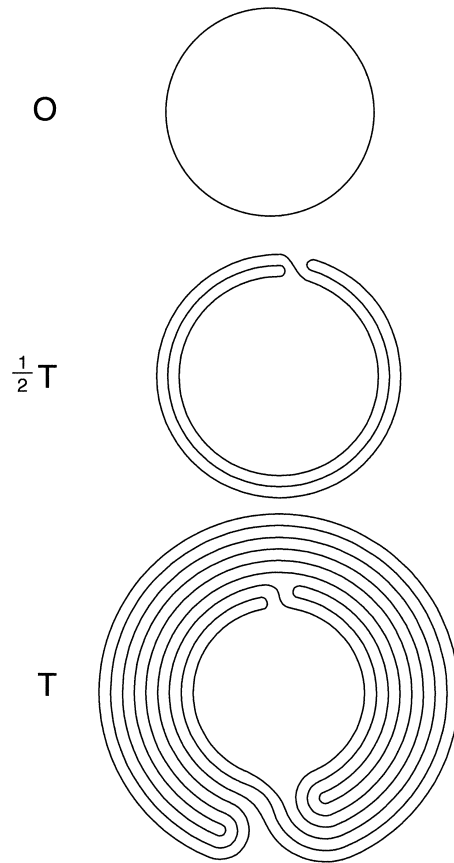


Fig. 5.12 What happens during each half of a full cycle in the van der Pol oscillator in terms of return maps. The flow along the cylinder is pinched out, deformed, and folded back to the cylinder during each half cycle. The deformations occur on opposite sides of the cylinder to respect the symmetry $(x, y, t) \rightarrow (-x, -y, t + \frac{1}{2}T)$. Each iterated stretch (by a factor of 3) and squeeze creates a total of nine branches.

As control parameters vary, the size of the pinched regions changes. It is possible to predict how new branches must be added to describe the chaotic dynamics as the pinched region becomes enlarged.

5.7 UNIQUENESS AND NONUNIQUENESS

Flow dynamics are conveniently represented by limits, or cartoons. This cartoon is a branched manifold. Branched manifolds were originally introduced to describe the unique organization of all the unstable periodic orbits in hyperbolic strange attractors. They also succinctly describe the stretching and squeezing mechanisms that generate strange attractors.

Many apparently different branched manifolds predict the same spectrum of orbits and the same topological organization (spectrum of linking numbers) of these orbits. Thus, there is not a 1:1 correspondence between branched manifolds and flow dynamics. This is somewhat analogous to the representation theory of groups. A single group can have many different inequivalent 1:1 (faithful) representations. In some sense, the group is fundamental and the matrix representations are simply a convenient means of performing computations. In the same way, the dynamics is fundamental and branched manifolds are convenient ways for doing calculations and classifying dynamics.

Definition: Two branched manifolds are **flow equivalent** if they predict the same spectrum of periodic orbits and these orbits have the same topological organization.

At the simplest level, a single branched manifold can have many different algebraic representations. An algebraic representation is obtained by projecting a branched manifold $\mathcal{BM} \subset R^3$ onto a plane $R^2 \subset R^3$. Different projections give different algebraic representations.

Definition: Two branched manifolds are **projection equivalent** if their algebraic representation differs only through their projection.

More generally, branched manifolds for the same flow can be geometrically different structures. The geometric differences can be due either to local moves or to global moves. A theory seems to exist to describe the equivalence of geometrically distinct branched manifolds under local moves. At present, there seems to be no theory to describe the equivalence of geometrically distinct branched manifolds under global moves.

In the first subsection we describe the local moves that can be used to transform one branched manifold into a geometrically different but flow-equivalent branched manifold. In the second subsection we describe three flow-equivalent branched manifolds that differ by global moves.

5.7.1 Local Moves

Knots and links remain invariant under a small number of Reidemeister moves. Braids remain invariant under the two types of braid relations that define braid groups. In the same way, branched manifolds remain invariant under a small number of local moves. These moves are:

- Branch line twists
- Writhe–twist exchange

- Branch line reversal
- Concatenation of inflows or outflows
- Branch line splitting

These moves are illustrated in Fig. 5.13.

In Fig. 5.13(a) we show two inflow branches joined at a branch line to an outflow branch. If the branch line is given half a twist in the clockwise direction, as shown in the middle of Fig. 5.13(a), the two inflow branches have their local torsion changed by $+1$ and the outflow branch will have its local torsion changed by -1 . In addition, the order in which the two inflow branches are joined at the branch line is reversed. If an additional half twist is given to the branch line (right), the local torsion of the incoming and outgoing branches is again changed by ± 1 , the order of joining is again reversed, and in addition the two incoming branches have their linking number increased by $+1$. Thus, the effect of a full twist on a branch line is that the local torsion of the incoming branches is changed by $+2$ and that of the outgoing branch is changed by -2 , the linking number of the two incoming branches is changed by $+1$, and the order in which the incoming branches is joined at the branch line is unchanged. Twisting in the opposite direction changes all signs.

Figure 5.13(b) shows how writhe and twist can be exchanged; this was described earlier. In Fig. 5.13(c) we show how interchanging the spatial position of two branch lines will force a full twist into a branch connecting these branch lines. The direction of the twist depends on whether branch a moves in front of or behind branch b .

In Fig. 5.13(d) and (e) we show that orbit organization is unchanged by the concatenation of inflows with inflows or outflows with outflows. In Fig. 5.13(d) we show how the order of two branch lines can be exchanged. In fact, it is sometimes convenient to draw the branched manifold with degenerate branch lines, as shown. In Fig. 5.13(e) we show that splitting points can also be concatenated. This representation is convenient when the stretch in a local region of phase space is larger than a factor of 2. In fact, it is useful to show a branch line feeding $[\exp(\lambda_1)] + 1$ branches in regions of phase space where the maximum local Lyapunov exponent is λ_1 ($[x]$ is the integer part of x).

In Fig. 5.13(f) we extend the inflow to the splitting point back beyond the nearest branch line into the two inflows that join at the branch line. This does not affect any periodic orbits, since no inverse image of any splitting point lies on a periodic orbit.

5.7.2 Global Moves

In Fig. 5.14 we show three geometrically inequivalent branched manifolds that are flow equivalent. The first is the branched manifold that holds all the closed magnetic field lines produced by a current flowing in a wire tied into the shape of a figure 8 knot. This branched manifold holds aesthetic appeal since it manifestly exhibits a rotation symmetry. This branched manifold has eight branches, which may be labeled $a\alpha$, ab , and so on. The incidence matrix shows the connectivity of these branches; for example, $a\beta$ is not an allowed transition.

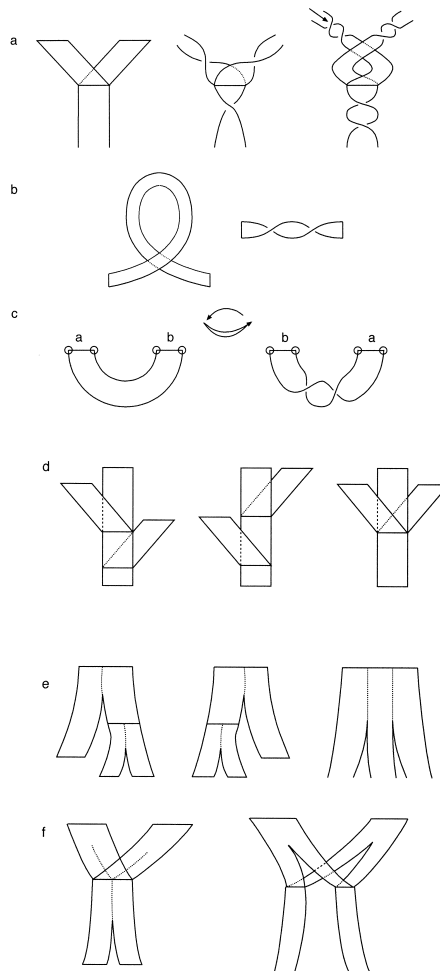


Fig. 5.13 Branched manifolds are flow equivalent under the following local moves. (a) The branch line is given a half twist. The inflow branches have their local torsion changed by $+1$, the outflow branch local torsion is changed by -1 , and the order in which the inflow branches are joined at the branch line is reversed. When the branch line is given a full twist, the order of joining is unchanged. However, the local torsion of the inflow and outflow branches is changed by $+2$ and -2 , and in addition the inflow branches link each other with a linking number $+1$. (b) Writhe and twist can be exchanged. (c) Interchanging the location of branch lines introduces a full twist into branches connecting them. (d) Topological organization is respected by interchanging the order of inflows. It is sometimes convenient to make the branch line degenerate. (e) Concatenated splitting charts can be treated the same way. This is convenient when the local Lyapunov exponent is larger than $\ln 2$. (f) The splitting point is extended backward beyond the nearest branch line in its past.

Table 5.1 Linking numbers for orbits to period 3 on the three representation of figure 8 flow dynamics

	$\alpha\beta$	αa	βb	$\alpha a \alpha \beta$	$\alpha a b a$	$\alpha \beta b a$	$\alpha \beta b \beta$	$\beta b a b$
	ab					$\beta \alpha a b$		
	x, y, z	xy	yz	x^2y	xy^2	xyz	y^2z	yz^2
	0, 1, 2	01	12	0 ² 1	01 ²	012	1 ² 2	12 ²
0, 1, 2	0	0	0	0	0	0	0	0
01	0	-1	0	-1	-1	-1	0	0
12	0	0	1	0	0	1	1	1
0 ² 1	0	-1	0	-2	-1	-1	0	0
01 ²	0	-1	0	-1	-2	0	0	0
012	0	-1	1	-1	-1	0	1	1
1 ² 2	0	0	1	0	0	1	2	1
12 ²	0	0	1	0	0	1	1	2

The second branched manifold shown in Fig. 5.14 was computed in [84]. There are again eight branches. The incidence matrix shows that the only transition not allowed is xz . The third branched manifold is flow equivalent to the second; both have the same spectrum of periodic orbits with the same topological organization. However, this third representation of the flow dynamics has a hole in the middle. This feature automates the computation of linking numbers.

With two exceptions, there is a 1:1 correspondence between the periodic orbits of the branched manifolds in Fig. 5.14(a) and (b). The two orbits $\alpha\beta$ and ab correspond to the three period-1 orbits x, y , and z , while the two orbits $\alpha\beta b a$ and $\beta\alpha a b$ correspond to the single period-3 orbit xyz . There is a 1:1 correspondence between the periodic orbits of the two branched manifolds shown in Fig. 5.14(b) and (c). Table 5.1 provides the linking numbers for the closed orbits up to period 3 on these three flow-equivalent branched manifolds.

For some purposes, it is convenient to simplify the description of the dynamics by expressing the branched manifold shown in Fig. 5.14(c) as a subbranched manifold of one showing a *full shift*. This idea is illustrated in Fig. 5.15. In the full-shift case, all periodic orbits based on three symbols are possible, including orbits containing the symbol sequence $\dots 02 \dots$. Such orbits do not occur in the branched manifold shown in Fig. 5.15(a).

For convenience, we show the return map for four branched manifolds in Fig. 5.16. Figure 5.16(a) provides the return map (tent map) for a Smale horseshoe template. Figure 5.16(b) and (c) provide the return maps for the two branched manifolds shown in Fig. 5.15. Figure 5.16(d) provides the return map for a branched manifold with four branches, of which branch 1 is orientation reversing. In each case the expansion is uniform. In three cases the branched manifold is fully expanding: case (b) is not.

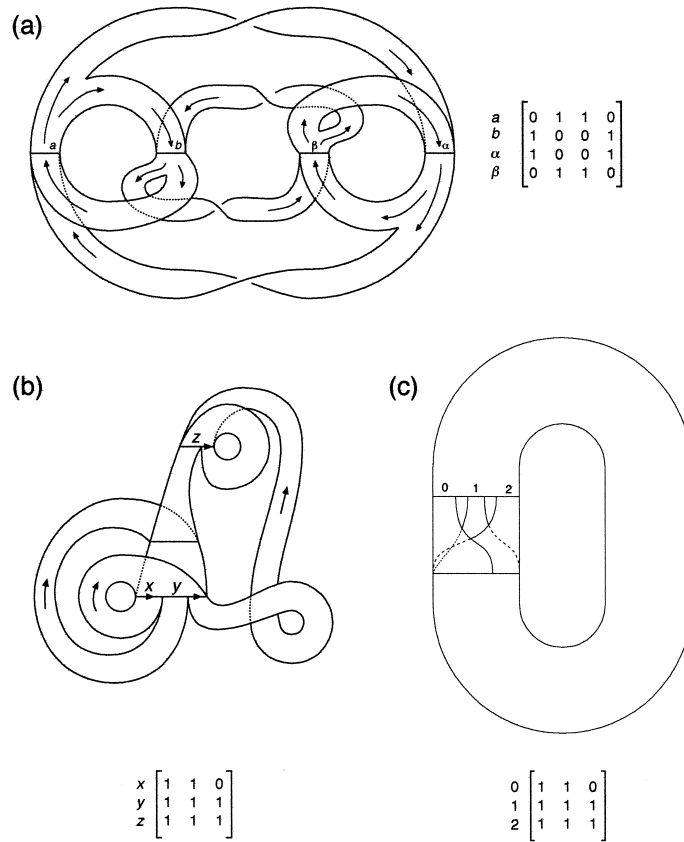


Fig. 5.14 (a) The branched manifold that describes the organization of all the closed magnetic field lines generated by a current-carrying wire tied into the shape of a figure 8 knot has eight branches. In this representation it manifests the rotational symmetry of the figure 8 knot. (b) The direct model of this branched manifold is simpler to deal with. The two branched manifolds are flow equivalent. With two exceptions, there is a 1:1 correspondence between periodic orbits on these two branched manifolds. (c) This third branched manifold is flow equivalent to the first two. It has a hole in the middle. This greatly simplifies the problem of computing the linking numbers for all the periodic orbits in the flow. The incidence matrices are given for each of these branched manifolds. The algebraic description of the third is given explicitly. Adapted with permission from Birman and Williams [84].

5.8 STANDARD FORM

By using the moves described in Section 5.3, any branched manifold can be transformed, after projection to R^2 , into the standard form shown in Fig. 5.17 [96, 97].

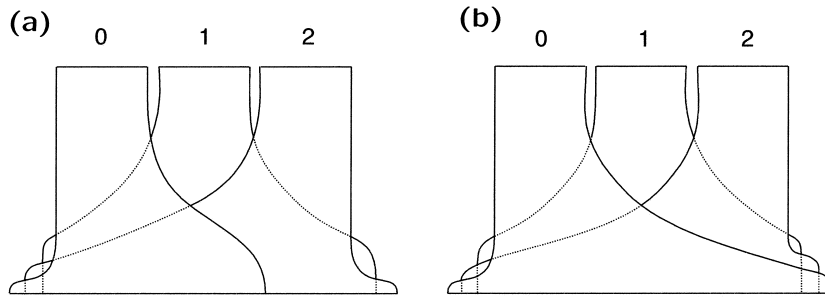


Fig. 5.15 The branched manifold (a) is a subtemplate of the one in (b). Some orbits on the right-hand branched manifold do not exist on the left-hand template. Those that exist on the subtemplate are organized in exactly the same way as their counterparts on the right.

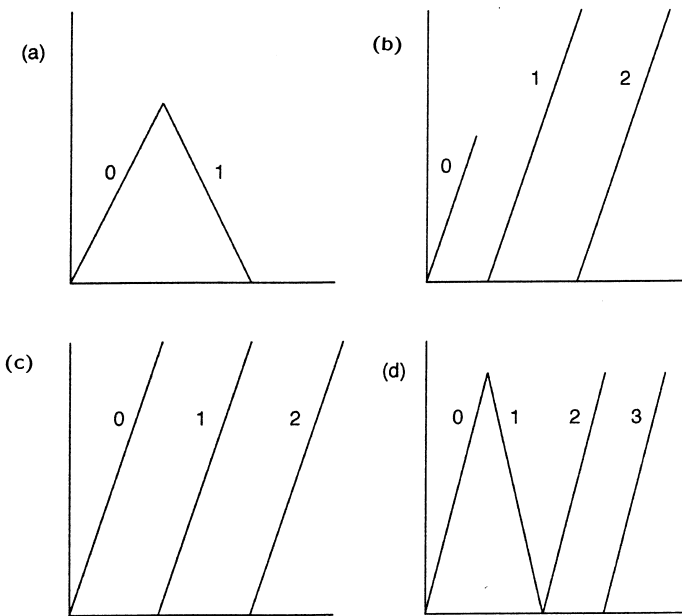


Fig. 5.16 Return maps for four branched manifolds. In each case the expansion is uniform. (a) The two branch Smale horseshoe template has a return map that is a tent map. (c) The three branch template shown in Fig. 5.15(b) is fully expanding, whereas (b) the subtemplate shown in Fig. 5.15(a) is not. (d) The four-branch template has one orientation-reversing branch.

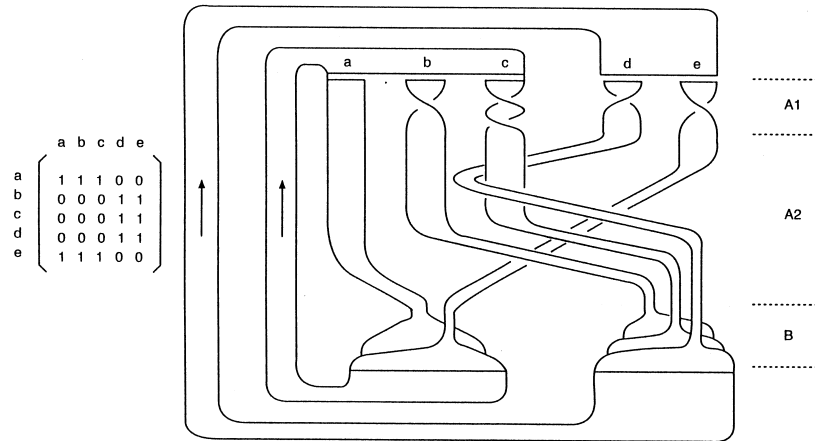


Fig. 5.17 Useful standard form for branched manifolds. All twisting occurs in region A1 and all crossing occurs in region A2. This information is summarized in a topological matrix T . All squeezing occurs in region B. This information is summarized in an array A . A Markov transition matrix (shown on the left for this template) shows how the branches are connected.

Each branch line is divided into segments by locating preimages of each tear point on the branch lines. The return flow from each branch line (bottom) feeds the segments of the branch lines (top). The stretch and squeeze mechanisms that generate chaos are described as follows:

- Branches twist but do not cross in the region labeled A1. The twists are assigned integer values $0, \pm 1, \pm 2, \dots$ in the same way as for knots: The twist of a branch is the signed number of crossings of the edges of that branch.
- Branches cross but do not twist in the region labeled A2. The crossings are assigned integer values $0, \pm 1, \pm 2, \dots$ in the same way as for knots by shrinking each branch down to a single curve. The information contained in regions A1 and A2 is summarized algebraically by a topological matrix T .
- Branches are squeezed together in the region labeled B. One convention is that the integers indicating ordering are larger the farther from the observer (i.e., increasing from top to bottom). The information contained in region B is summarized in array A .
- A Markov transition matrix is introduced to identify which branches are connected to which.

5.9 TOPOLOGICAL INVARIANTS

Linking numbers for any pair of periodic orbits on a branched manifold can be computed. The computation depends only on the algebraic description of the branched manifold. The computations simplify considerably when the branched manifold has a hole in the middle. That is, much simplification occurs when a series of local or global moves can be exploited to transform the branched manifold to a form in which all the stretching and squeezing is represented between two branch lines that are identified by a return flow which neither stretches nor squeezes. This representation for a branched manifold is particularly convenient because each trip around the hole in the middle corresponds to one period. Such a flow has one Poincaré section, which can be taken as the branch line. We describe the systematics of linking number computations for branched manifolds of this type below.

5.9.1 Kneading Theory

When only one branch line is present, it is possible to define an order along this branch line. We adopt the convention that the order increases from left to right. We assume that the branched manifold has n branches, labeled $0, 1, 2, \dots, n - 1$ from left to right, for lack of imagination. We also assume for convenience that the incidence matrix is full (cf. Fig. 5.15). This causes no problem: We can simply ignore periodic orbits that are forbidden by the original incidence matrix.

Under these conditions every orbit of minimal period p is represented by a symbol sequence $(\sigma_1\sigma_2 \cdots \sigma_p)^{\infty}$, or

$$\sigma_1\sigma_2 \cdots \sigma_p \ \sigma_1\sigma_2 \cdots \sigma_p \ \cdots$$

After one period the symbol sequence advances to

$$\sigma_2 \cdots \sigma_p \sigma_1 \ \sigma_2 \cdots \sigma_p \sigma_1 \ \cdots$$

Advancing by a period amounts to cyclic permutation of the symbols (*symbolic dynamics*).

We now wish to locate periodic orbits on the branched manifold. We do this by computing the “address,” or “zip code,” along the branch, for each of the p initial conditions of a period p orbit.

The address along the branch line is computed as follows:

1. Write out the symbol code for one of the initial conditions. For example:

$$\sigma_1\sigma_2 \cdots \sigma_p \ \sigma_1\sigma_2 \cdots \sigma_p \ \cdots$$

2. Conjugate each symbol following passage through an orientation-reversing branch. Orientation-reversing branches are branches that twist through an odd multiple of π radians. These branches have negative parity, where the parity

of branch i is defined as $\mathcal{P}(i) = (-1)^{T_{ii}}$ and T_{ii} is the appropriate element of the topological matrix. The conjugate of σ_i is $\bar{\sigma}_i$, where

$$\sigma_i + \bar{\sigma}_i = n - 1 \tag{5.6}$$

3. This process produces a symbol sequence of period either p or $2p$, depending on whether the orbit goes through an even or odd number of orientation-reversing branches. The symbol sequence is the address, in normal numerical order, for the initial condition along the branch line.
4. This process is repeated for the remaining initial conditions of the period- p orbit.

Example: Assume that we have a template with four branches 0, 1, 2, 3, and branch 1 is orientation reversing [cf. Fig. 5.16(d)]. To find the address of 0213 along the branch line, we perform the following simple calculation:

$$\begin{aligned} 0213 \ 0213 \ 0213 \ \dots &\rightarrow 021\bar{3} \ \bar{0}\bar{2}\bar{1}\bar{3} \ 021\bar{3} \ \dots \\ &= 0210 \ 3123 \ 0210 \ \dots \end{aligned} \tag{5.7}$$

This is repeated three more times for the additional three initial conditions. The four addresses for the passage of this period-4 orbit through the branches of this four-branch manifold have period 8:

Initial Condition	Address	Fraction Base 10	Decimal	
0213	0210 3123	9435/65535	0.143969	(5.8)
2130	2103 1230	37740/65535	0.575875	
1302	1031 2302	19890/65535	0.303502	
3021	3021 0312	51510/65535	0.785992	

Every point on a branch line is the address for an initial condition for some orbit through the branched manifold. The address may be represented by a symbol string: $a_1 a_2 a_3 \dots$. Two possibilities arise:

Irrational: The symbol string is never repeating. Such symbol strings represent irrational numbers and nonrepeating (chaotic) orbits.

Rational: The symbol string is eventually repeating. Such symbol strings represent rational numbers and orbits that are either periodic, finite, or eventually periodic.

Periodic orbits of period p are described by a repeating sequence of p symbols $(\sigma_1 \sigma_2 \dots \sigma_p)^\infty$, as described above. The address is a symbol sequence of period p or $2p$. We compute the rational fraction for a single case, then present the general result. On the Smale horseshoe template with orientation-preserving branch 0 and

orientation-reversing branch 1, the period-3 orbit $(011)^\infty$ has a period-3 address $(010)^\infty$. The rational fraction for this address is

$$\begin{aligned}
 010\ 010\ 010\ \dots &\rightarrow \frac{0}{2} + \frac{1}{2^2} + \frac{0}{2^3} + \frac{0}{2^4} + \frac{1}{2^5} + \frac{0}{2^6} + \frac{0}{2^7} + \frac{1}{2^8} + \frac{0}{2^9} + \dots \\
 &\rightarrow (0 \times 2^2 + 1 \times 2^1 + 0 \times 2^0) \left(\frac{1}{2^3} + \frac{1}{2^6} + \frac{1}{2^9} + \dots \right) \\
 &= \frac{0 \times 2^2 + 1 \times 2^1 + 0 \times 2^2}{1 \times 2^2 + 1 \times 2^1 + 1 \times 2^2} = \frac{010}{111}
 \end{aligned} \tag{5.9}$$

This calculation has been done in the binary system. To be strictly accurate, we should write the exponents 2, 3, 4, 5, . . . as 10, 11, 100, 101, Conversion to the more familiar decimal system is simple:

$$\frac{010}{111} \rightarrow \frac{0 \times 2^2 + 1 \times 2^1 + 0 \times 2^2}{1 \times 2^2 + 1 \times 2^1 + 1 \times 2^2} = \frac{2}{7} = 0.285714\ 285714\ \dots \tag{5.10}$$

For the more general case, of a periodic address on an n -branched manifold, the result proceeds in a similar fashion. The “ n -imal” rational fraction address for the period-4 orbit 0213 described above is $(0210\ 3123)/(3333\ 3333)$, where $3333\ 3333 = 4^8 - 1$. This fraction is easily converted to base 10 and its decimal equivalent:

$$0213 \rightarrow 0210\ 3123 \rightarrow \frac{0210\ 3123}{3333\ 3333} \rightarrow \frac{9435}{65535} \rightarrow 0.1439688716 \tag{5.11}$$

These results are summarized for the four initial conditions of this orbit in Eq. (5.8).

Finite orbits are orbits that reach a splitting point on a branch after a finite number of periods. Splitting points are initial conditions for flows to a fixed point. The address for a finite orbit is a finite symbol sequence. Splitting points for templates with two, three, and four branches are shown in Fig. 5.16. For the three fully expansive branched manifolds shown in this figure, with two, three, and four branches, the addresses of the splitting points are $\frac{1}{2}$; $\frac{1}{3}$ and $\frac{2}{3}$; and $\frac{1}{4}$, $\frac{2}{4}$, and $\frac{3}{4}$; respectively. For the nonfully expanding template, the addresses are $\frac{2}{8}$ and $\frac{5}{8}$.

We illustrate the basic idea by computing the itinerary of the finite orbit 3212 on the four-branch manifold discussed above, whose return map is shown in Fig. 5.16(d).

Initial Condition	Address	Fraction	
3212	3211	$\frac{3}{4^1} + \frac{2}{4^2} + \frac{1}{4^3} + \frac{1}{4^4}$	(5.12)
212	211	$\frac{2}{4^1} + \frac{1}{4^2} + \frac{1}{4^3}$	
12	11	$\frac{1}{4^1} + \frac{1}{4^2}$	
2	2	$\frac{2}{4^1}$	

Eventually periodic orbits are represented by symbol sequences that eventually become periodic. As an example, the orbit with symbol sequence $(01)^2(011)^\infty$ on

the Smale horseshoe template settles down to a period-3 orbit after four periods. The address for this initial condition is

$$\begin{aligned}
 01\ 01\ 011\ 011\ \dots &\rightarrow 01\ 10\ 010\ 010\ 010 \\
 &\rightarrow \frac{0}{2^1} + \frac{1}{2^2} + \frac{1}{2^3} + \frac{0}{2^4} + \frac{0}{2^5} + \frac{1}{2^6} + \frac{0}{2^7} + \frac{0}{2^8} + \frac{1}{2^9} + \frac{0}{2^{10}} + \dots \\
 &= \frac{0110}{10000} + \frac{1}{10000} \frac{010}{111} \\
 &= \frac{6}{2^4} + \frac{1}{2^4} \frac{2}{7} \rightarrow 0.39\overline{285714}^\infty
 \end{aligned}
 \tag{5.13}$$

We summarize these results now for a branched manifold with n branches, a full incidence matrix, and uniform expansion along the branch. It is convenient to express results in a number system based on n and the corresponding n -imal fractions in the interval $[0, 1]$ of the branch line.

1. There is a 1:1 correspondence between irrational numbers and initial conditions for chaotic orbits.

2a. There is a 1:1 correspondence between n -mal fractions of the form

$$\frac{\text{integer}}{n^p - 1} \quad \text{or} \quad \frac{\text{integer}}{n^{2p} - 1}
 \tag{5.14}$$

and initial conditions for orbits of period p .

2b. There is a 1:1 correspondence between n -mal fractions of the form

$$\frac{\text{integer}}{n^k}
 \tag{5.15}$$

and initial conditions for finite orbits of k periods.

2c. There is a 1:1 correspondence between all other n -mal fractions, which have the form

$$\frac{\text{integer}}{n^k} + \frac{1}{n^k} \times \frac{\text{integer}}{n^p - 1} \quad \text{or} \quad \frac{\text{integer}}{n^k} + \frac{1}{n^k} \times \frac{\text{integer}}{n^{2p} - 1}
 \tag{5.16}$$

These fractions describe orbits that settle down to period- p orbits after k transient periods.

The irrationals are dense on the interval. So also are (separately) all fractions of the form (5.14), (5.15), and (5.16). As a result:

1. Chaotic orbits are dense on branched manifolds.

2a. Periodic orbits are dense on branched manifolds.

2b. Finite orbits are dense on branched manifolds.

2c. Eventually periodic orbits are dense on branched manifolds.

These denseness statements hold when the branched manifold is blown back up to the original strange attractor.

5.9.2 Linking Numbers

Once the locations of periodic orbits on a branched manifold have been determined, computation of the linking numbers is simply a matter of counting crossings. We illustrate by computing the linking number of the orbits 01 and 011 on a Smale horseshoe template. The results of the computation are shown in Fig. 5.18.

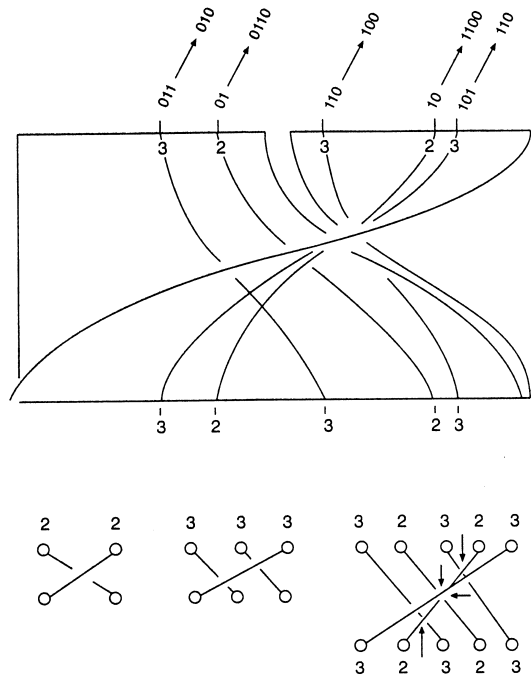


Fig. 5.18 Initial conditions for period-2 orbit 01 and period-3 orbit 011 on the Smale horseshoe template are computed in Eq. (5.18). These two orbits are draped over the interesting part of this branched manifold. The linking and self-linking numbers are computed by counting crossings. For these orbits, $SL(01) = +1$, $SL(011) = +2$, and $L(01, 011) = +2$.

The period-2 orbit 01 goes through the orientation reversing branch 1 once. Therefore the addresses of its two initial conditions have period 4. The period-3 saddle 011 goes through the orientation-reversing branch twice, so its three initial conditions

have period 3. The addresses, and corresponding decimal fractions, are:

Initial Condition	Address	Decimal Fraction
01	01 10	6/15
10	11 00	12/15
011	010	2/7
110	100	4/7
101	110	6/7

(5.17)

These five addresses are shown along the branch line of the Smale horseshoe template. The order of these initial conditions is simple to read off from either the binary representation or the decimal fraction:

$$\frac{010}{2/7} < \frac{01\ 10}{2/5} < \frac{100}{4/7} < \frac{11\ 00}{4/5} < \frac{110}{6/7} \tag{5.18}$$

Computing the linking numbers is now simply a matter of counting crossings. The self-linking numbers of the period-2 and period-3 orbits are $SL(01) = +1$ and $SL(011) = +2$. The computation is shown at the bottom of Fig. 5.17. The computation of the linking number $L(01, 011) = \frac{1}{2}(1 + 1 + 1 + 1) = +2$ is also shown at the bottom of Fig. 5.18. Computation of linking numbers on branched manifolds with a hole in the middle have been reduced to a FORTRAN code, which is available at the authors' Web site.

5.9.3 Relative Rotation Rates

Computation of relative rotation rates follows a very similar algorithm. Two orbits of periods p_A and p_B are draped over a branched manifold. Two initial conditions are joined by an oriented line segment, and the number of half twists that this segment undergoes as it evolves through $p_A \times p_B$ periods is counted. This integer is divided by $2 \times p_A \times p_B$. This calculation is repeated for all other initial conditions. This bookkeeping has also been reduced to a FORTRAN code, which is available at the Web site listed above. The inputs are the same as for the linking number computation. The output is a table of relative rotation rates.

The computation can be simplified using the procedure introduced in Section 4.3.2. That is, it is sufficient to construct a $(p_A + p_B) \times (p_A + p_B)$ crossing matrix C which summarizes the crossing information in the nontrivial part of the branched manifold. A cyclic permutation matrix P must also be constructed. This indicates how the initial conditions from one period are mapped to the initial conditions for the next. Then it is sufficient to construct the matrix [cf. Fig. 4.17].

$$RRR = \frac{1}{2 \times p_A \times p_B} \sum_{k=1}^{p_A \times p_B} P^{-k} C P^k \tag{5.19}$$

The p_a^2 matrix elements of the upper diagonal $p_A \times p_A$ matrix are the self-relative rotation rates for orbit A , and similarly for orbit B . The $p_A \times p_B$ matrix elements of either of the two off-diagonal matrices are the relative rotation rates of orbit A with orbit B .

5.10 ADDITIONAL PROPERTIES

Branched manifolds have a number of additional properties that we have not yet discussed. We describe a number of these properties below.

5.10.1 Period as Linking Number

It is often a simple matter to define the period of a closed orbit. For example, in driven dynamical systems the (dynamical) period of a closed orbit is an integer multiple of the driving period. Specifically, it is the number of distinct intersections of the orbit with a Poincaré section. This remains true when the phase space has the structure of a torus: $R^2 \times S^1$.

In more complicated cases it is not quite so obvious how to define the period of a closed orbit. For example, what is the period of a closed orbit on the Figure 8 branched manifold?

The period of a nontrivial closed orbit must always be a positive integer. There is a natural way to construct integers from closed orbits. This involves computation of linking numbers. Thus, it should be no surprise that it is always possible to define a topological period of a closed orbit on a branched manifold as the linking number of that orbit with some reference closed orbit which does not intersect the branched manifold. Then the topological period of a closed orbit A with respect to the reference loop is [84]

$$\text{topological period}(A) = LN(\text{Ref}, A) \tag{5.20}$$

where Ref is the reference loop. For the figure 8 branched manifold, one reference loop may be taken as the figure 8 knot itself. Other reference loops can also be used.

On the figure 8 branched manifold shown in Fig. 5.19, the closed orbits ab and $\alpha\beta$ each have topological period 1, while the closed loops $a\alpha$ and $b\beta$ each have period 2.

5.10.2 EBK-like Expression for Periods

Computing the topological period of a closed orbit on the figure 8 branched manifold can be simplified by deforming the reference loop. Such a deformation is shown in Fig. 5.19. The reference loop consists of the figure 8 knot itself. The deformed loop consists of a union of four loops. One each surrounds the branch lines b and β , one each surrounds the branches $a\alpha$ and αa . Then the period of any closed loop is the sum of the linking numbers of that loop with the four loops resulting from deformation of the figure 8 knot.

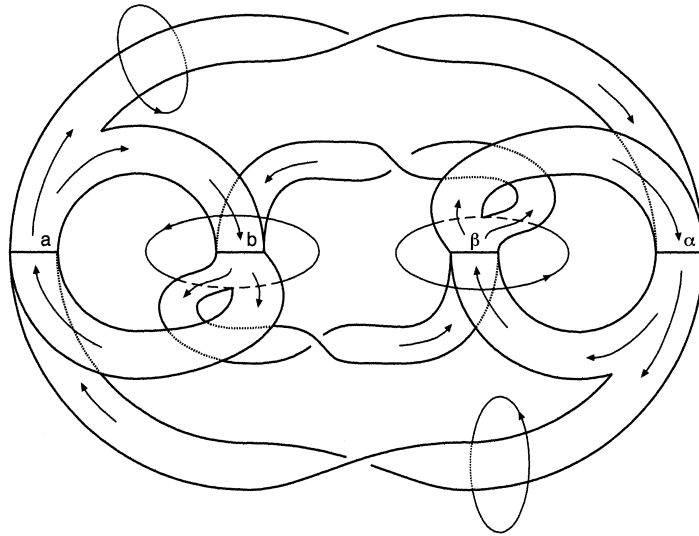


Fig. 5.19 The figure 8 knot is deformed to the union of four much simpler loops. This greatly simplifies computation of the topological period of any closed orbit on the branched manifold of the figure 8 knot. Adapted with permission from Birman and Williams [84].

This argument is general. We can deform the reference orbit for any branched manifold and write it as the union of “fundamental loops”: $\text{Ref} \rightarrow \cup_i C_i$. We can then write the topological period of any closed orbit A as the sum of the linking numbers of A with each of the fundamental loops C_i :

$$\text{period}(A) = LN(\cup_{i=1} C_i, A) = \sum_{i=1} LN(C_i, A) \tag{5.21}$$

This result is very similar to the Einstein–Brillouin–Keller (EBK) quantization formula. The phase change of a single-valued wavefunction around any closed loop in its configuration space must be an integer multiple of 2π . The phase change is an action integral, so that

$$\oint_L p dq = \oint_{\sum_i m_i C_i} p dq = \sum_i m_i \oint_{C_i} p dq \tag{5.22}$$

The integrals around the closed loops C_i are themselves quantized:

$$\frac{1}{2\pi\hbar} \oint_{C_i} p dq = n_i + \frac{1}{4}\beta_i \tag{5.23}$$

Here both n_i and β_i are integers. The integer β_i is the Maslov index for the loop. The integers n_i have a natural interpretation as quantum numbers.

The loops C_i in (5.21) must be chosen as a basis set in the sense that every closed orbit A satisfies $LN(C_i, A) \geq 0$, at least one of these linking numbers is positive for each A , and inequivalent closed orbits A and B have inequivalent linking numbers with the basis loops C_i .

5.10.3 Poincaré Section

Poincaré introduced an ingenious idea to reduce the study of n -dimensional flows to the study of $(n - 1)$ -dimensional maps. The idea is to introduce $(n - 1)$ -dimensional surface(s) into the phase space. The surfaces are called variously the *Poincaré surface*, the *surface of section*, the *Poincaré section*, and so on. These surfaces have the property that the flow is transverse to the surface, always meets the surface from the same side, and almost all initial conditions meet the surface of section a countable number of times.

It is possible to define a Poincaré surface for any flow that satisfies the conditions of the Birman–Williams theorem. We first define the Poincaré section for the semiflow $\bar{\Phi}_t$ on the branched manifold $\mathcal{B}\mathcal{M}$. The Poincaré section is simply the union of the branch lines:

$$\text{Poincaré section} = \cup \text{branch lines} \tag{5.24}$$

For the figure 8 branched manifold the Poincaré section is the union of the four branch lines $a, b, \beta,$ and α : $\text{Poincaré section} = a \cup b \cup \beta \cup \alpha$.

To construct the Poincaré section for the original flow, we “undo” the original Birman–Williams projection. This blowing-up process is described in more detail below. Briefly, each branch line is expanded against the stable direction to form a disk or rectangle. The expansion must be sufficient to ensure that the flow under $\bar{\Phi}_t$ in the neighborhood of the branch line intersects the disk or rectangle. Then the Poincaré section for the original flow is the union of the disks obtained by blowing up the branch lines of $\mathcal{B}\mathcal{M}$.

5.10.4 Blow-Up of Branched Manifolds

It is often useful to “inflate” or “blow up” a branched manifold in order to get a better approximation of the original dynamics. This is done by expanding the branch lines to “branch rectangles” against the strongly contracting direction. In a sense, this reverses the Birman–Williams projection.

We illustrate this process in Fig. 5.20. To do this, the negative Lyapunov exponent, whose limit is $-\infty$ in the construction of the branched manifold, is allowed to be finite. The stretch and squeeze factors for the map $R^2 \rightarrow R^2$ are then $\mu = \pm e^{\lambda_1}$ and $\nu = \pm e^{\lambda_3}$, with $|\mu| > 1 > |\nu| > 0$.

Periodic orbits in the map $R^2 \rightarrow R^2$ can be located by a method somewhat more involved than the kneading theory construction. Forward and backward iterates of the map are constructed. Their intersection defines a fractal in R^2 . This construction is carried out explicitly for the two-branch mapping associated with a Smale horseshoe in Section 2.10. The intersections of the forward and backward iterates provide

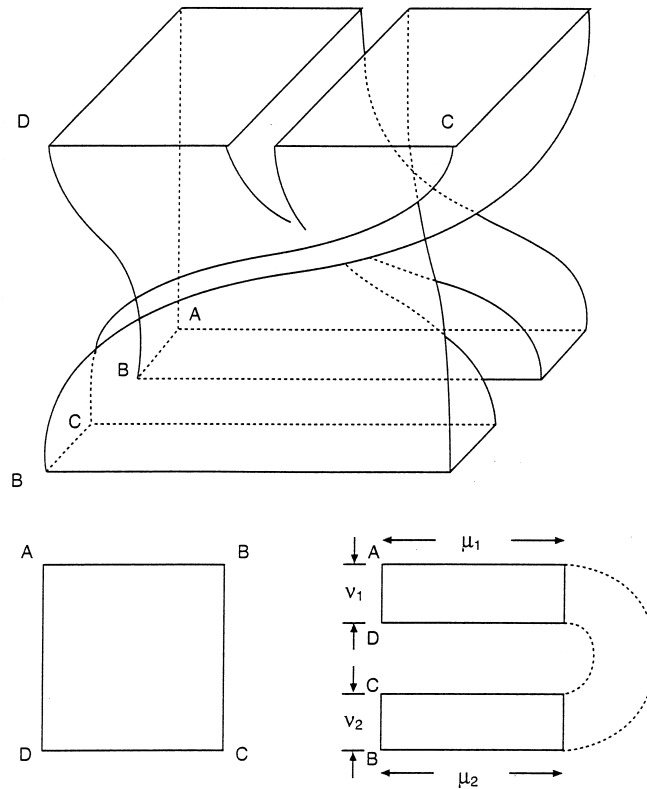


Fig. 5.20 A two-branch template is inflated by expanding against the contracting direction. The result provides an invertible map $R^2 \rightarrow R^2$.

addresses for all orbits in the flow and map. Needless to say, topological invariants remain invariant under inflation.

We should point out here, forcefully, that the fractal structure of a strange attractor comes about from repetition of the stretching and and squeezing processes in phase space. If one knows the topological structure of the attractor, as exemplified by its branched manifold, it is possible to compute geometric quantities such as Lyapunov dimension and fractal dimensions, simply by inputting the positive and negative Lyapunov exponents λ_1 and λ_3 , or else a distribution of values for the local Lyapunov exponent $\lambda_1(x)$ and $\lambda_3(x)$. In this sense, the topological structure (branched manifold) is fundamental, the Lyapunov exponents are inputs, and all geometric invariants are derived quantities. From the geometric quantities alone, it is not possible to

make any statements about stretching and squeezing mechanisms, much less about the branched manifold, which defines and classifies the dynamics.

5.10.5 Branched-Manifold Singularities

A two-dimensional branched manifold has two types of singularities. These are of dimension 0 and 1. The zero-dimensional singularity is a splitting point. This point describes stretching mechanisms. The one-dimensional singularity is the branch line. This line describes squeezing mechanisms. Between them, these two singularities describe the processes that build up a strange attractor in R^3 .

Things are not quite as simple in higher dimensions. For starters, there is no Birman–Williams theorem. However, it is still possible to carry out a Birman–Williams projection (5.1). In the simple case where $\lambda_1 > \lambda_2 > \lambda_3 = 0 > \lambda_4$ and $\lambda_1 + \lambda_2 + \lambda_3 + \lambda_4 < 0$, the identification (5.1) maps the flow to a three-dimensional structure. This is a manifold almost everywhere. Its three directions correspond to the two stretching directions and the flow direction. However, it is not a manifold because it contains singularities. Singularities occur with dimension 0, 1, and 2. We do not have a clearcut identification of singularities with the stretching and squeezing processes.

5.10.6 Constructing a Branched Manifold from a Map

It is sometimes necessary to reconstruct properties of a flow simply from a return map. We illustrate how this can be done, using a simple example.

We consider here a map that has a period-3 orbit. The intersections of this orbit with a Poincaré section are s_1, s_2, s_3 , and under the flow $s_1 \rightarrow s_3 \rightarrow s_2 \rightarrow s_1$. The map, and the folding that it forces, are shown in Fig. 5.21(a).

Other representations of this flow are possible. A second is shown in Fig. 5.21(b). Here the cyclic permutation is expressed as the composition of two interchanges: $(s_1, s_2, s_3) \rightarrow (s_2, s_1, s_3) \rightarrow (s_2, s_3, s_1)$. The branched manifold that describes this process is shown in Fig. 5.21(c). A return map on the interval $(s_1 s_2 s_3)$ is given in Fig. 5.21(d).

5.10.7 Topological Entropy

The incidence matrix provides information about the connectivity of a branched manifold. Equivalently, it provides information about which paths through the branched manifold are allowed and which are not. It is very useful to label the rows and columns of the incidence matrix by branch lines. This was done to describe the connectivity of the branched manifold for the figure 8 knot in terms of a 4×4 matrix [cf. Fig. 5.14(a)]. Although this is sometimes useful, it is often inadequate. For example, the Smale horseshoe template has one branch line, which would yield a 1×1 incidence matrix. What *is* sufficient is the following. Extend each splitting point back to the nearest branch line in its past. Then each branch line is the union of a small number of pieces. Under this construction, the branch line for the Smale

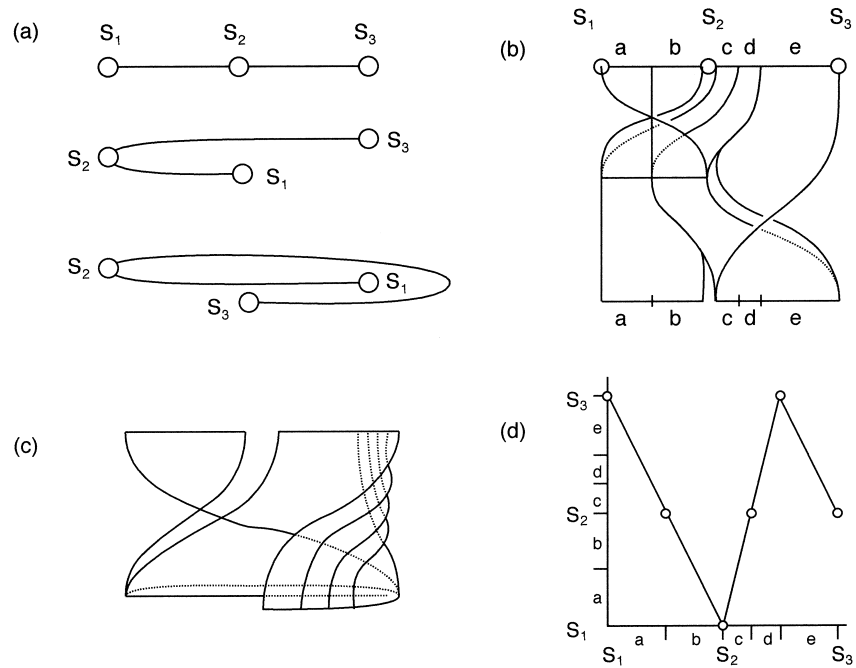


Fig. 5.21 Two ways to construct a branched manifold from a map. (a) The deformation of the line joining the three points of the period-3 orbit is shown. (b) The deformation of the line segment is carried out in two steps. The first interchanges s_1 and s_2 , the second interchanges s_1 and s_3 . (c) This branched manifold describes the deformation. (d) The return map for the branch line onto itself is shown. Adapted with permission from Birman and Williams [84].

horseshoe template has two pieces, while each of the four branch lines in Fig. 5.14(a) has two components. The incidence matrix for the Smale horseshoe is the full 2×2 matrix $\begin{pmatrix} 1 & 1 \\ 1 & 1 \end{pmatrix}$, and that for the template of the figure 8 knot is a sparse 8×8 matrix. In general, we adopt the smallest suitable incidence matrix.

The matrix element $(I^2)_{ik}$ describes the number of distinct ways it is possible to travel from branch i to branch k in two steps,

$$(I^2)_{ik} = \sum_j I_{ij} I_{jk} \tag{5.25}$$

For the branched manifold in Fig. 5.14(c),

$$\begin{pmatrix} 1 & 1 & 0 \\ 1 & 1 & 1 \\ 1 & 1 & 1 \end{pmatrix}^2 = \begin{pmatrix} 2 & 2 & 1 \\ 3 & 3 & 2 \\ 3 & 3 & 2 \end{pmatrix} \tag{5.26}$$

This shows, for example, that there are two ways to go from branch y to branch z :

$$\begin{array}{llll} y \rightarrow x \rightarrow z & \text{No} \\ y \rightarrow y \rightarrow z & \text{Yes} \\ y \rightarrow z \rightarrow z & \text{Yes} \end{array} \tag{5.27}$$

More generally, $(I^p)_{ik}$ is the number of distinct ways of going from i to k in p distinct steps. If $i = k$, $(I^p)_{ii}$ is the number of distinct ways of starting and ending at branch i in p distinct steps.

If each step is one period, then $(I^p)_{ii}$ is the number of distinct ways of starting and ending at branch i in p periods. For the matrix I^2 above, we find seven ways of going around the branched manifold and getting back to the starting point in two periods:

$$\begin{array}{llll} x \rightarrow x \rightarrow x & y \rightarrow x \rightarrow y \\ x \rightarrow y \rightarrow x & y \rightarrow y \rightarrow y & z \rightarrow y \rightarrow z \\ & y \rightarrow z \rightarrow y & z \rightarrow z \rightarrow z \end{array} \tag{5.28}$$

Three of these involve period-1 orbits iterated twice. The remaining four paths are

$$\begin{array}{ll} x \rightarrow y \rightarrow x & \text{and} \quad y \rightarrow x \rightarrow y \\ y \rightarrow z \rightarrow y & \text{and} \quad z \rightarrow y \rightarrow z \end{array} \tag{5.29}$$

The two paths $x \rightarrow y \rightarrow x$ and $y \rightarrow x \rightarrow y$ belong to the single period-2 orbit $(xy)^\infty$. Similarly for the paths $y \rightarrow z \rightarrow y$ and $z \rightarrow y \rightarrow z$, which are the paths of $(yz)^\infty$ through the branched manifold starting from the two initial conditions. The number of distinct period-2 orbits on this branched manifold is

$$N(2) = \frac{1}{2} [\text{tr}(I^2) - N(1)] = \frac{1}{2}(7 - 3) = 2 \tag{5.30}$$

where $N(1) = 3$ is the number of period-1 orbits: $N(1) = \text{tr}(I)$.

The number of orbits of minimal period p , $N(p)$, is given by

$$pN(p) = \text{tr}(I^p) - \sum_{k \text{ divides } p} kN(k) \tag{5.31}$$

The subtraction removes orbits that are of period p but not of *minimal* period p . Such orbits are of period p which “go around” m times, where $p/k = m$ (integer, $m \geq 2$).

This algorithm is simple to implement. The only input is a suitable incidence matrix. In Table 5.2 we show the number of distinct closed orbits of minimal period p , $N(p)$, for the Smale horseshoe template and the two branched manifolds shown in Fig. 5.15.

Caution: This spectrum is sometimes presented differently. Many orbits of period p are saddle node pairs. Such pairs are often counted as a single orbit (type). In the Smale horseshoe template the period-3 saddle node pair 001 and 011 is counted as one orbit type. The period-4 saddle node pair 0001 and 0011 is counted as one, while the orbit 0111, period-doubled daughter of 01, is counted as another. Since 5 is prime, the six period-5 orbits are counted as three saddle-node pairs. At period 6, one orbit (001 011) is the period-doubled daughter of 001; the remaining eight comprise four saddle-node pairs. The number 7 is prime, while at period 8 there are the daughter of 0001 and the daughter of 0111 (itself the daughter of 01, . . .), giving $2 + \frac{1}{2}(30 - 2) = 16$ orbit (types) of period 8. With this type of counting, the spectrum of orbit types of periods 1, 2, 3, 4, 5, 6, 7, 8, . . . on the Smale horseshoe template is 1, 1, 1, 2, 3, 5, 9, 16,

Inspection of Table 5.2 reveals that the number of orbits of period p increases rapidly with p . In fact, the increase is exponential. We can write

$$N(p) \sim e^{ph_T} \tag{5.32}$$

where h_T is the topological entropy. This number can be estimated directly from the incidence matrix.

Here is how. If the eigenvalues of I are $\lambda_1 > \lambda_2 > \dots > \lambda_n$, then

$$\begin{aligned} \text{tr}(I) &= \lambda_1 + \lambda_2 + \dots + \lambda_n \\ \text{tr}(I^p) &= \lambda_1^p + \lambda_2^p + \dots + \lambda_n^p \end{aligned} \tag{5.33}$$

For p large and $\lambda_1 > \lambda_2$, $\lambda_1^p \gg \lambda_2^p$ and, to a good approximation, $\text{tr}(I^p) \sim \lambda_1^p$. In addition, the terms $kN(k)$ which are subtracted from $\text{tr}(I^p)$ in (5.31) are of the order of $(\lambda_1)^k$, $k \leq p/2$. As a result, they can be neglected, and

$$N(p) \simeq \frac{1}{p}(\lambda_1)^p \simeq e^{ph_T} \tag{5.34}$$

Taking logarithms, we find that

$$h_T = \ln(\lambda_1) - \frac{1}{p} \ln(p) \xrightarrow{p \rightarrow \infty} \ln(\lambda_1) \tag{5.35}$$

We provide the approximation $(\lambda)^p/p$ for orbits up to period 9 for the three cases discussed in Table 5.2. For the two fully expanding templates, the incidence matrix has rank 1, with eigenvalues 2, 0 and 3, 0, 0. In these cases, $N(p) \sim 2^p/p$ and $3^p/p$. In the third case, the incidence matrix has rank 2 with two nonzero eigenvalues $\frac{1}{2}(3 \pm \sqrt{5})$. Then $N(p) \sim (2.618)^p/p$. In this case it is seen that the correction of the second eigenvalue to $\text{tr}(I^p) = \lambda_+^p + \lambda_-^p \rightarrow (2.618)^p + (0.382)^p$ becomes insignificant as p becomes large ($p = 2$, for example). It is also clear that the subtraction $-\sum kN(k)$ has the smallest effect for p prime (i.e., $p = 3, 5, 7$) and the largest effect when p is the smallest number with the largest number of prime factors. Thus, $N(p) \simeq \lambda^p/p$ is a worse approximation for $p = 8 = 2^3$ than for $p = 9 = 3^2$.

Table 5.2 Number of closed orbits up to period 9 in three different branched manifolds^a

Incidence Matrix	1	2	3	4	5	6	7	8	9
$\begin{pmatrix} 1 & 1 \\ 1 & 1 \end{pmatrix}$	2	1	2	3	6	9	18	30	56
	2.0	2.0	2.7	4.0	6.4	10.7	18.3	32.0	56.9
$\begin{pmatrix} 1 & 1 & 0 \\ 1 & 1 & 1 \\ 1 & 1 & 1 \end{pmatrix}$	3	2	5	10	24	50	120	270	640
	2.6	3.4	6.0	11.7	24.6	53.7	120.4	275.9	642.0
$\begin{pmatrix} 1 & 1 & 1 \\ 1 & 1 & 1 \\ 1 & 1 & 1 \end{pmatrix}$	3	3	8	18	48	116	312	810	2184
	3.0	4.5	9.0	20.2	48.6	121.5	312.4	820.1	2187.0

^aTop row, exact; bottom row, λ^p/p .

5.11 SUBTEMPLATES

Topological invariants of orbits and orbit pairs are unchanged under control parameter variation as long as the orbits exist. However, as control parameters are varied, periodic orbits are created and/or annihilated. Therefore, it is not obvious that the topological description of a strange attractor is invariant under control parameter variation.

5.11.1 Two Alternatives

In fact, there are two options, which will be illustrated with respect to both the Rössler and Lorenz attractors. Suppose that the Rössler equations are integrated for control parameter values for which there is a strange attractor, and that all the unstable periodic orbits in the attractor are constructed from an alphabet with two symbols, 0 and 1. If every possible symbol sequence is allowed, the attractor is hyperbolic. We have never encountered such an attractor, either in simulations of dissipative systems or in the analysis of experimental data. In our experience, it is always the case that some symbol sequences are forbidden.

For example, if the symbol sequence 00 is the only symbol sequence that is forbidden, every periodic orbit is constructed from a vocabulary with the two words $a = 01$ and $b = 1$. The flow, projected down onto a standard Smale horseshoe branched manifold, does not extend over the entire branched manifold, as can be seen in Fig. 5.22(a). The Markov transition matrix for the original two-letter alphabet consisting of 0 and 1 changes

$$\text{from } M = \begin{bmatrix} 1 & 1 \\ 1 & 1 \end{bmatrix} \quad \text{to} \quad M = \begin{bmatrix} 0 & 1 \\ 1 & 1 \end{bmatrix} \quad (5.36)$$

The part of the Smale horseshoe template that is not traversed by the projection of the flow (the semiflow) is shown shaded in Fig. 5.22(a). It is constructed by observing that the flow must never enter the left quarter of the branch line shown at the top, for this encodes 00. Therefore, the two preimages of this part of the branch line must be removed, as well as all the preimages of their preimages. What remains is a fractal subset of the original branched manifold.

An alternative representation of this dynamics is given by the branched manifold shown in Fig. 5.22(b). This is a *subtemplate* of the original two-branch template shown in Fig. 5.22(a). The two branches $a = 01$ and $b = 1$ represent flows through (a) branches 0 followed by 1 in the Smale horseshoe template, and (b) through branch 1 in that template. All possible sequences involving the two words a and b are allowed. The Markov transition matrix for this subtemplate is full. However, constructing the subtemplate of Fig. 5.22(b) from the original shown in Fig. 5.22(a) is not easy—it borders on nightmarish even for this simple case.

The subtemplate of Fig. 5.22(b) describes dynamics at the creation of the period-3 orbit 3_1 . For other parameter values other vocabularies and grammars describe the dynamics. In general, the number of words required grows with the wordlength. For example, to wordlength 4 the required words might be 01, 011, and 0111. In general, as longer and longer symbol sequences occur, new inadmissible sequences appear. We can take this into account by increasing the number of words in the vocabulary. Then in this representation of the dynamics:

- The subtemplate can in principle be constructed from the original template.
- It typically has an infinite number of branches.
- The number of branches corresponding to words of finite length is finite.
- Every possible sequence of words is allowed.

We are faced with a similar choice with another branched manifold. The flow generated by the Shimizu–Morioka equations [2, 98] is similar to the flow generated by the Lorenz equations [cf. Fig. 5.8(c) with Fig. 8.5]. However, the former occupies a subtemplate of the latter. The restriction of the Shimizu–Morioka flow on a Lorenz template is shown in Fig. 5.23(a). On the original Lorenz template, some periodic orbits are allowed and others forbidden. This corresponds to the fact that some symbol sequences are forbidden in the Shimizu–Morioka flow. One possibility is to restrict the projection of the flow to the part of the branched manifold that is shaded. Another is to construct a subtemplate representing a vocabulary of allowed words which can occur in arbitrary order. Such a subtemplate is shown in Fig. 5.23(b). Once again, constructing this simple subtemplate from the original Lorenz template borders on the nightmarish.

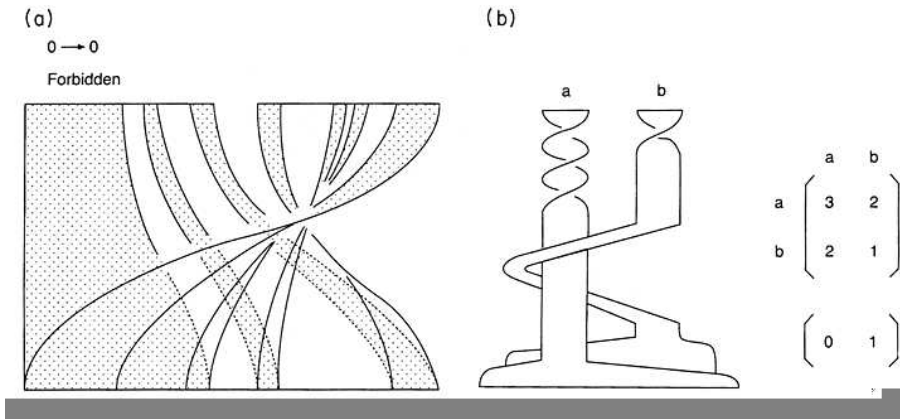


Fig. 5.22 (a) When the only forbidden symbol sequence 00, the flow is restricted to the unshaded part of the Smale horseshoe template. Some orbits on the original template are allowed; others are forbidden. The forbidden region consists of all preimages of the left quarter of the upper branch. (b) The flow can be represented by this subtemplate of the Smale horseshoe template when only the symbol sequence 00 is forbidden.

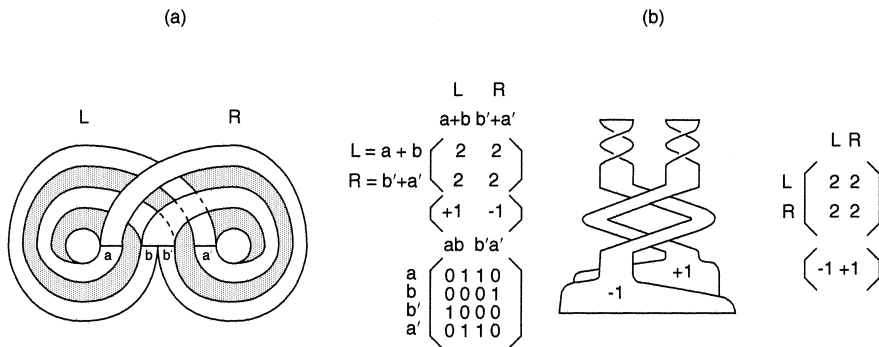


Fig. 5.23 (a) The flow generated by the Shimizu–Morioka equations is restricted to the shaded subset of the Lorenz template. (b) All orbits in the Shimizu–Morioka strange attractor can be represented by this subtemplate of the original Lorenz template.

5.11.2 A Choice

The two alternatives for representing dynamics that have been presented above are summarized as follows:

1. As control parameters are varied, the basic template remains and describes all the unstable periodic orbits in the strange attractor, and then some. Some of the orbits predicted to exist by the template do not exist—they have been “pruned away.” All that remain are organized as they were in the hyperbolic limit.
2. As control parameters are varied, the dynamics is represented by a series of subtemplates. The vocabulary changes from one control parameter to another, as does the template. In general, the subtemplates have an infinite number of branches, but all possible word sequences are allowed.

Of these two alternatives, we adopt the first without hesitation, for the following reasons:

- The template is invariant, or at least robust, under control parameter variation.
- It is much easier to see how the flow gets “pushed around” on a template than to work out how one subtemplate metamorphoses into another as control parameters vary.
- With only one template to work with, the topological invariants of all orbits need to be computed only once. As long as those orbits remain in existence as the attractor changes with the control parameters, these quantities remain invariant.
- It makes no sense to force an interpretation in terms of subtemplates to preserve an idea of hyperbolicity or full-shift dynamics when this is nongeneric in dissipative physical systems in the first place.
- The global organization of a flow is largely determined by its fixed points and their insets and outsets, and by some low-period orbits and their stable and unstable manifolds. Since these are robust under large variations in parameter values, we also want the caricature (template) to be robust under these variations.

With this interpretation, templates are topological invariants under change of coordinates and initial conditions. They are robust under change of control parameter values. That is, they can remain unchanged under large changes of the control parameter values. However, under sufficiently large changes in control parameter values, they can change (cf. Chapter 9). They can change by adding new branches. They can change also if the flow ceases to visit branches. In any case, the template must change when the basic alphabet required for a symbolic encoding of the dynamics undergoes a change.

The changing nature of the dynamics over a fixed template can be described as follows, using the Lorenz template as an example. The two segments of the branch lines L and R are divided into n_1 and n_2 segments L_1, L_2, \dots, L_{n_1} and R_1, R_2, \dots, R_{n_2} . Then the linking numbers (topology) depend only on the symbol name ($LRL L \dots$), but the dynamics depend on the $(n_1 + n_2) \times (n_1 + n_2)$ Markov transition matrix. This matrix describes, to some extent (the better the larger n_1 and n_2) which orbits are allowed in the flow and which have been pruned from the flow.

5.11.3 Topological Entropy

The problem of computing topological entropy for a map or a (semi)flow over a branched manifold is simple when the Markov transition matrix describes allowed and forbidden period-1 processes. Specifically, the topological entropy is the logarithm of the largest real root of this matrix.

If time steps of varying length are the basic units, the problem of computing topological entropy becomes more interesting. Since chaotic dynamics is described in terms of letters, vocabularies, and grammars, it might be expected that there is some nontrivial relation between the concepts of chaos and those of communication. This hope is not in vain: There is a strong connection. Many of the major problems were formulated and answered by Shannon in his seminal contributions to communications theory [44, 45]. We first present Shannon's results for communication channels. Then we map these results to dynamical systems theory.

The capacity of a transmission channel is

$$C = \lim_{T \rightarrow \infty} \frac{1}{T} \log N(T)$$

Here $N(T)$ is the number of allowed signals of duration T and \log is to base e . First, assume that an alphabet contains n symbols S_1, S_2, \dots, S_n of lengths t_1, t_2, \dots, t_n , and that every possible symbol sequence is allowed. The number of symbol sequences of length t is

$$N(t) = N(t - t_1) + N(t - t_2) + \dots + N(t - t_n)$$

A well-known result from the theory of finite difference equations states that $N(t)$ is asymptotic to AX_0^t , where A is a constant and X_0 is the largest real solution of the characteristic equation

$$X^t = X^{t-t_1} + X^{t-t_2} + \dots + X^{t-t_n}$$

or, equivalently,

$$1 = X^{-t_1} + X^{-t_2} + \dots + X^{-t_n}$$

We assume that all words in the vocabulary have integer length and that there are $w(1)$ words of length 1, $w(2)$ words of length 2 (i.e., they are two symbols long in the original alphabet), and so on. Then the characteristic equation for this vocabulary and grammar is

$$1 = \sum_{p=1}^{\infty} \frac{w(p)}{X^p} \tag{5.37}$$

The topological entropy is the logarithm of the largest real root of this equation.

In many grammars, not all symbol sequences are allowed (qu is OK but qv is KO). In such cases, assume that there are m states b_1, b_2, \dots, b_m . For each state only certain symbols from the set S_1, S_2, \dots, S_n can be transmitted (different subsets for different states). The transmission of symbol S_k from state b_i to state b_j (b_i may be the same as b_j) takes time $t_{ij}^{(k)}$. This process is illustrated by a graph such as that shown in Fig. 2.17.

Theorem: The channel capacity C is $\log X_0$, where X_0 is the largest real root of the $m \times m$ determinantal equation

$$\det \left| \sum_k X^{-t_{ij}^{(k)}} - \delta_{ij} \right| = 0 \tag{5.38}$$

We now translate these results into statements useful for computing the topological entropy for a dynamical system. The table that effects the isomorphism between topological entropy for dynamical systems and channel capacity for communication systems is

Communication Systems	Dynamical Systems
Graph	Branched manifold
S_i	Branch
t_i	Period
b_j	Branch line
Channel capacity	Topological entropy

Remark: Assume that a dynamical system is described by a branched manifold with m branches and incidence matrix I . Transit through each branch takes one period. Then (5.38) becomes

$$\det \left[\frac{1}{X} I_{ij} - \delta_{ij} \right] = X^{-m} \det [I_{ij} - X \delta_{ij}] = 0$$

As a result, in this case the topological entropy is the logarithm of the largest real eigenvalue of the incidence matrix I .

In the following two subsections we consider a series of applications of the expressions (5.37) and (5.38) for topological entropy to subtemplates of the Smale horseshoe template and subtemplates involving branches describing the dynamics seen in circle maps.

5.11.4 Subtemplates of the Smale Horseshoe

In the following three examples the alphabet has the two letters 0 and 1. The grammar is full. It is just the words that differ from one example to the next.

Example 1: There are two words: $S_1 = 0$ and $S_2 = 1$, $t_1 = t_2 = 1$, and (5.37) becomes

$$1 = \frac{1}{X} + \frac{1}{X}$$

The solution is $X_0 = 2$, $h_T = \log 2 = 0.693147$.

Example 2: There are again two words, $S_1 = 1$ and $S_2 = 01$. Then $t_1 = 1$ and $t_2 = 2$, so (5.37) becomes

$$1 = \frac{1}{X} + \frac{1}{X^2}$$

The solution is $X_0 = \frac{1}{2}(1 + \sqrt{5})$, $h_T = 0.481212$.

Example 3: There are four words: 01, 011, 0111, and 01111. All combinations of these symbol sequences are allowed, and (5.37) becomes

$$1 = \frac{1}{X^2} + \frac{1}{X^3} + \frac{1}{X^4} + \frac{1}{X^5}$$

The solution is $X_0 = 1.534158$, $h_T = 0.427982$.

5.11.5 Subtemplates Involving Tongues

Some dynamical systems do not follow a simple stretch and fold route to chaos as exhibited by the Rössler system. The best known of these is the van der Pol oscillator, but it is one of many dissipative systems that follow an alternative route. In this route a Hopf bifurcation occurs, followed eventually by some kind of transition to chaos. The inertial manifold has the topology of a hollow donut: $(I^1 \times S^1) \times S^1$. In this topology the second S^1 parameterizes a periodic driving term. A Poincaré section is easily defined. In a Poincaré section the intersection $I^1 \times S^1$ is topologically an annulus (I^1 is an interval). By the Birman–Williams theorem this projects down to a one-dimensional set that is topologically a circle (S^1). The return map is then a map of the circle to itself. The properties of the circle map were summarized in Section 2.12.

Invertibility is lost when the circle folds over on itself during the return map. Because of the boundary conditions (S^1 is topologically different from R^1), two folds must occur. The flow from S^1 to its folded over image is described by a three-branch manifold. Branches L and R are orientation preserving. On branch L the rotation angle increases by less than 2π , on branch R it increases by more than 2π . Branch C occurs between the two folds and is orientation reversing.

While the circle map is still invertible, mode locking occurs. Each mode-locked region is characterized by a rational fraction $\omega = p/q$, with $0 \leq \omega \leq 1$ for the case of zero global torsion. In the rational fraction, q is the number of times the orbit goes around the long circumference of a torus and p is the number of times it goes around the short circumference: q is the period and p is the winding number.

The symbol sequence of the saddle-node pair in the Arnol'd tongue p/q is $W(1)W(2) \cdots W(q)$, where

$$W(i) = \left[i \times \frac{p}{q} \right] - \left[(i-1) \times \frac{p}{q} \right] = \begin{pmatrix} 0 \\ 1 \end{pmatrix} \longrightarrow \begin{pmatrix} W(i) = L \\ W(i) = R \end{pmatrix}$$

where $[x]$ is the integer part of x . For $p/q = \frac{3}{5}$, $W(1)W(2)W(3)W(4)W(5) \rightarrow LRLRR$. The partner orbit is obtained by replacing the penultimate symbol by C (e.g., $LRLCR$).

Chaotic behavior occurs when the map loses the invertibility property and the Arnol'd tongues begin to overlap. We describe the chaotic behavior when tongues described by rational fractions $\omega_1 = p_1/q_1$ and $\omega_2 = p_2/q_2$ just begin to overlap. We assume that $\omega_1 < \omega_2$ and

$$\det \begin{bmatrix} p_1 & p_2 \\ q_1 & q_2 \end{bmatrix} = \pm 1$$

At this point the behavior is chaotic and the vocabulary contains three words. These are:

- A The symbol sequence for the left-hand tongue p_1/q_1
- B The symbol sequence for the right-hand tongue p_2/q_2
- \overline{B} The partner of B

Not every symbol sequence is allowed, for \overline{B} must be preceded by A . Each word labels a branch in a branched manifold. This is a subtemplate of the branched manifold that describes the dynamics in the fully expansive case (L , R , and C have a fully expansive incidence matrix). The incidence matrix for the three words A , B , and \overline{B} is

$$\begin{matrix} A \\ B \\ \overline{B} \end{matrix} \begin{bmatrix} 1 & 1 & 1 \\ 1 & 1 & 0 \\ 1 & 1 & 0 \end{bmatrix}$$

Applying this information to Eq. (5.38), we find that

$$\det \begin{bmatrix} \frac{1}{X^{q_1}} - 1 & \frac{1}{X^{q_1}} & \frac{1}{X^{q_1}} \\ \frac{1}{X^{q_2}} & \frac{1}{X^{q_2}} - 1 & 0 \\ \frac{1}{X^{q_2}} & \frac{1}{X^{q_2}} & -1 \end{bmatrix} = 0$$

This reduces to

$$X^{q_1+q_2} - X^{q_1} - X^{q_2} - 1 = 0 \quad \text{or} \quad \frac{1}{X^{q_1}} + \frac{1}{X^{q_2}} + \frac{1}{X^{q_1+q_2}} = 1$$

Example 1: Compute the vocabulary and the topological entropy for the strange attractors that occur when the tongues p_1/q_1 and p_2/q_2 just overlap, for the pairs $(\frac{1}{2}, \frac{2}{3})$, $(\frac{1}{2}, \frac{3}{5})$, $(\frac{3}{5}, \frac{2}{3})$.

p_1/q_1	p_2/q_2	A	$\frac{B}{\overline{B}}$	X_0	h_T
$\frac{1}{2}$	$\frac{2}{3}$	LR	LRR LCR	1.429108	0.357051
$\frac{1}{2}$	$\frac{3}{5}$	LR	$LRLRR$ $LRLCR$	1.307395	0.268037
$\frac{3}{5}$	$\frac{2}{3}$	$LRLRR$	LRR LCR	1.252073	0.224801

Example 2: Compute the topological entropy for the low-period Arnol'd tongues for which $p_1q_2 - q_1p_2 = \pm 1$. *Solution:* The results depend only on the periods q_1 and q_2 . To period 9, here they are. Entries for which the periods are not relatively prime have been left blank.

	3	4	5	6	7	8	9
2	0.357051		0.268037		0.219131		0.187366
3		0.253442	0.224801		0.186002	0.172048	
4			0.196620		0.164136		0.142458
5				0.160664	0.148188	0.137920	0.129277
6					0.135847		
7						0.117680	0.110713
8							0.103803

5.12 SUMMARY

Branched manifolds were introduced by Birman and Williams [83, 84] as a simple tool to describe completely the organization of all the unstable periodic orbits in the Lorenz dynamical system [83]. Their theorem guarantees that branched manifolds can be used to describe the organization of unstable periodic orbits in any three-dimensional dissipative dynamical system with a (hyperbolic) strange attractor. However, one of the first branched manifolds discussed in detail by Birman and Williams, the figure 8 knot-holder, describes the topological organization of all the closed magnetic field lines generated by a constant current flowing in a wire knotted into a figure 8 shape [84]. This is a conservative dynamical system. It is not clear that the Birman–Williams theorem can be applied *only* to dissipative systems.

As stated, the Birman–Williams theorem is not immediately useful for the analysis of chaotic data. Two of the input assumptions are too restrictive. Both assumptions (hyperbolicity, three-dimensional flow) can be relaxed. Once these modifications were made, the Birman–Williams theorem became a key component in the topological analysis of chaotic data and the classification of strange attractors.

We have described the branched manifolds for the four standard testbeds of dynamical systems theory: the Duffing, van der Pol, Lorenz, and Rössler attractors. Each branched manifold has an algebraic representation in terms of three matrices. The topological matrix T determines how the various branches twist and cross each other. The joining array A identifies the order in which two or more branches are joined at a branch line. The transition or incidence matrix I determines the flow ordering: which branches flow into which other branches.

The location of periodic orbits on branched manifolds can be determined by kneading theory. Once orbits have been located, their linking numbers and relative rotation rates can be determined algorithmically. The inputs to the algorithm are the two matrices T and A . Conversely, a symbolic coding of the orbits in a flow determines I , and information about the linking numbers of these orbits can be used to construct

the two matrices T and A . The result is that branched manifolds can be identified on the basis of properties of unstable periodic orbits identified in the flow.